

On the accuracy of mass and size measurements of young protoplanetary disks

Eduard I. Vorobyov^{1,2,3,*}, Aleksandr M. Skliarevskii³, Vardan G. Elbakyan^{4,3}, Michael Dunham⁴ and Manuel Güdel¹

¹University of Vienna, Department of Astrophysics, Türkenschanzstrasse 17, 1180, Vienna, Austria;

²Institut für Astro- und Teilchenphysik, Universität Innsbruck, Technikerstraße 25, 6020 Innsbruck, Austria

³Research Institute of Physics, Southern Federal University, Rostov-on-Don 344090, Russia;

⁴Fakultät für Physik, Universität Duisburg-Essen, Lotharstraße 1, D-47057 Duisburg, Germany

⁵Department of Physics, Middlebury College, Middlebury, VT 05753, USA

Correspondence*:

Eduard Vorobyov

eduard.vorobiev@univie.ac.at

ABSTRACT

Knowing the masses and sizes of protoplanetary disks is of fundamental importance for the contemporary theories of planet formation. However, their measurements are associated with large uncertainties. In this proof of concept study, we focus on the very early stages of disk evolution, concurrent with the formation of the protostellar seed, because it is then that the initial conditions for subsequent planet formation are likely established. Using three-dimensional hydrodynamic simulations of a protoplanetary disk followed by radiation transfer postprocessing, we constructed synthetic disk images at millimeter wavelengths. We then calculated the synthetic disk radii and masses using an algorithm that is often applied to observations of protoplanetary disks with ALMA, and compared the resulting values with the actual disk mass and size derived directly from hydrodynamic modeling. We paid specific attention to the effects of dust growth on the discrepancy between synthetic and intrinsic disk masses and radii. We find that the dust mass is likely underestimated in Band 6 by factors of 1.4–4.2 when Ossenkopf & Henning opacities and typical dust temperatures are used, but the discrepancy reduces in Band 3, where the dust mass can be even overestimated. Dust growth affects both disk mass and size estimates via the dust-size-dependent opacity, and extremely low values of dust temperature (\approx several Kelvin) are required to recover the intrinsic dust mass when dust has grown to mm-sized grains and its opacity has increased. Dust mass estimates are weakly sensitive to the distance to the source, while disk radii may be seriously affected. We conclude that the accuracy of measuring the dust mass and disk radius during the formation of a protoplanetary disk also depends on the progress in dust growth. The same disk, but observed at different stages of dust growth and with different linear resolutions, can have apparent radii that differ from the intrinsic value by up to a factor of two. Multi-wavelength observations that can help to constrain the maximum dust size would be useful when inferring the disk masses and sizes.

Keywords: Protostellar disks, Protoplanetary disks, Hydrodynamics, Stars: formation, dust evolution

1 INTRODUCTION

Knowing the masses of protoplanetary disks is of fundamental importance for the contemporary theories of planet formation. The mass of gas in the disk influences its tendency to undergo gravitational instability and form planets through disk gravitational fragmentation (Mayer et al., 2007; Vorobyov, 2013; Nayakshin, 2017; Mercer and Stamatellos, 2020; Boss and Kanodia, 2023; Xu et al., 2025). The mass of dust in the disk sets the upper limits on the masses of terrestrial planets and cores of giant planets to be formed via planetesimal hierarchical growth or pebble accretion (Pollack et al., 1996; Lambrechts and Johansen, 2012; Jin and Li, 2014). Dust particles at the upper part of the size spectrum are the main carriers of dust mass in the disk (Birnstiel et al., 2016), but they also contribute strongly to the (sub-)millimeter opacity in the outer cold and gravitationally unstable disk regions if their size exceeds a certain threshold value (Pavlyuchenkov et al., 2019).

Knowing the sizes of protoplanetary disks is of no less importance for planet formation theories. Gravitational fragmentation is known to operate in the disk at distances beyond tens of astronomical units, because at smaller distances the high rate of shear and slow cooling prevents disk fragmentation (Gammie, 2001; Rice et al., 2003; Meru and Bate, 2012). The size of the dust disk, which is usually smaller than that of the gas disk (Ansdell et al., 2018; Trapman et al., 2019; Hsieh et al., 2024), carries information about the efficiency of radial dust drift and, indirectly, about the efficiency of dust growth in the system. The size of the dust disk also defines the spatial extent within which planetesimals – the first building blocks of protoplanets – are expected to form. Interestingly, recent observational data on FU Orionis-type objects revealed several features that do not fit into the contemporary models of disk evolution, dust growth, and planet formation, indicating that the disks of these outburst objects tend to be of a smaller size but higher mass than disks around their quiescent counterparts (Kóspál et al., 2021). The time evolution of both masses and sizes reflects the dominant transport and loss mechanisms of mass and angular momentum in a protoplanetary disk (Manara et al., 2023).

While the masses and sizes of the gas disk are usually obtained via the observations of CO isotopologues, sometimes complemented with N_2H^+ , or hydrogen deuteride (HD) (McClure et al., 2016; Trapman et al., 2025), the dust disk is probed via observations of thermal dust emission at (sub-)mm wavelengths (Tobin et al., 2020; Tychoniec et al., 2020; Anderson et al., 2022). Observational estimates of gas masses suffer from uncertainties in the abundance of gaseous tracers, their freezeout on dust grains, and strong dependence of population levels on the gas temperature (Bergin and Williams, 2017; Molyarova et al., 2017). Alternatively, dynamical measurements that involve fitting of the disk rotation curve to the Keplerian law can provide estimates on the gas mass in the disk (Veronesi et al., 2021), but such exercises require high resolution observations.

Estimates of dust mass in the disk are no less affected by uncertainties in the dust opacity, inclination, and dust temperature (Dunham et al., 2014; Tobin et al., 2020; Tychoniec et al., 2020), particularly, if the optically thin assumption is made. The latter may be justified for evolved Class II systems, but not for younger Class 0/I counterparts. The situation may become even more complicated in protostellar systems that are in their earliest stages of formation. Observationally, these objects may reveal themselves as very low luminosity objects or VELLOs (Dunham et al., 2010; Kim et al., 2019), which may be the first hydrostatic cores (FHSCs) surrounded by nascent

disks (Vorobyov et al., 2017a). Indeed, numerical hydrodynamics simulations indicate that a protoplanetary disk may start forming before the FHSC collapses due to molecular hydrogen dissociation to form the protostellar seed (Inutsuka, 2012; Tomida et al., 2015; Vorobyov et al., 2024).

In this work, we aim to determine the accuracy of the dust mass and disk radius measurements in a protoplanetary disk in its very early stages that are concurrent with the formation of the protostellar seed. This is important because this stage is likely to set the initial dust repository for subsequent planet formation. To this end, we produce synthetic observables of the protoplanetary disk made with a dust distribution derived from three-dimensional numerical hydrodynamics simulations of cloud collapse and disk formation. We also consider models with artificially imposed limits on the maximum dust size to account for electrostatic or bouncing barriers, which are not considered self-consistently in the dust growth model (Vorobyov et al., 2025). This allows us to connect numerical simulations with synthetic observations and test the basic assumptions underlying dust mass and disk radius estimates in real observations. In Sect. 2 the numerical hydrodynamics model is briefly reviewed. The methods to estimate disk masses and sizes from numerical data are described in Sect. 3. The main results are presented in Sect. 4. Model limitations and comparison with previous work are provided in Sect. 5. Main conclusions are summarized in Sect. 6.

2 NUMERICAL MODEL

In this section, we provide a basic description of the numerical hydrodynamics model employed to simulate the formation of a protoplanetary disk. We used the three-dimensional ngFEOSAD code to simulate the gravitational collapse of a pre-stellar cloud and early evolution of a nascent protoplanetary disk. The code solves the equations of gas and dust dynamics including self-gravity and dust growth in the polytropic approximation on nested Cartesian meshes. The detailed description of the code and the pertinent equations can be found in Vorobyov et al. (2024), and also in a concise form in Appendix 7. Here, we provide the basic information that is relevant to calculating the synthetic observables of our model protoplanetary disk.

The numerical simulations start from the gravitational collapse of a slowly rotating Bonnor-Ebert sphere with a mass of $0.87 M_{\odot}$. The initial temperature of the cloud is 10 K and it is given an initial positive density perturbation of 30% to initiate the collapse. The ratios of rotational-to-gravitational and thermal-to-gravitational energies are 0.5% and 70%, respectively. Initially, the dust-to-gas mass ratio is set equal to 1:100 and the maximum dust size is $a_{\max} = 2.0 \mu\text{m}$. The minimum dust size is kept fixed at $5.0 \times 10^{-3} \mu\text{m}$ and the slope of the dust size distribution is kept constant at $p = -3.5$ throughout the simulation for simplicity.

The dust-to-gas mass ratio throughout the computational domain begins to deviate from the initial value as collapse proceeds, the disk forms, and dust starts growing and settling to the disk midplane. Dust enhancement of the innermost cloud regions occur already in the predisk stage due to differential collapse of gas and dust in the cloud (Bate, 2022). Mild dust growth also occurs in the collapse stage (Vorobyov et al., 2025), but its main phase begins when the FHSC forms and the disk begins to build around the FHSC owing to conservation of angular momentum of infalling matter. We terminate the simulations just before the FHSC is about to collapse due to molecular hydrogen dissociation and to form the protostellar seed. We therefore address the very early stages of evolution when the luminosity of the central source is still low but the protoplanetary disk may

already have started to form. Considering these early stages of disk evolution also makes it easier to model the synthetic disk images because uncertainties with the luminosity and radius of a young stellar object are lifted (Vorobyov et al., 2017b). We note that while compact disks around FHSCs were theoretically and numerically predicted (Tomida et al., 2015; Wurster et al., 2021; Vorobyov et al., 2025), they are still observationally elusive. The more advanced stage when the central protostar reaches a mass of $0.1 - 0.2 M_{\odot}$ will be addressed in a follow-up study.

Relevant to our model are the choices of the turbulent viscosity $\alpha_{\text{visc}} = 10^{-3}$ and the dust collisional fragmentation velocity $v_{\text{frag}} = 5.0 \text{ m s}^{-1}$. The former influences the dust growth efficiency and maximum dust size via the turbulent relative velocity of dust-to-dust collisions (Ormel and Cuzzi, 2007), while the latter sets the fragmentation barrier and also the maximum dust size in our simplified monodisperse dust growth model (Birnstiel et al., 2012). We note that the drift barrier is self-consistently treated via the numerical solution of the dust dynamics equations with dust-to-gas friction, including the backreaction of dust on gas. The choices of α_{visc} and v_{frag} were motivated by observations of dust settling in protoplanetary disks (Rosotti, 2023) and laboratory experiments on dust survival during collisions (Gundlach and Blum, 2015; Blum, 2018). Apart from the actual dust size distribution obtained in our numerical simulations, we also consider several models in which the maximum dust size is artificially reset to smaller values to imitate the possible effects of electrostatic and bouncing barriers (Okuzumi, 2009; Wada et al., 2011), not considered self-consistently in ngFEOSAD (Vorobyov et al., 2025).

We used 12 nested grids with the linear size of the outermost grid equal to 0.09 pc. The number of grid cells per Cartesian coordinate direction of each nested grid is $N = 64$. The effective numerical resolution in the inner 4.5 au is 0.14 au and it remains at a sub-au level up to 36 au. The disk at the end of simulations extends to about 50-60 au.

3 ESTIMATES OF DISK MASSES AND SIZES

In this section, we describe the method we used to derive the disk masses and sizes directly from our numerical hydrodynamics simulations. We also explain how we obtained synthetic observables of the protoplanetary disk with a radiation transfer tool and used these observables to compare the synthetic disk masses and sizes with those derived directly from hydrodynamic modeling.

3.1 Deriving the disk mass and size from hydrodynamic simulations

The first step in our procedure is to derive the disk mass using the three-dimensional distribution of gas densities and velocities in our computational domain. To do that in a numerical model that self-consistently computes the cloud-to-disk transition, we have to develop a means of distinguishing the disk from the infalling cloud. For this purpose, we adopted the disk tracking conditions outlined in Joos et al. (2012). In particular, we used the following criteria to determine if a particular computational cell in the entire computational domain belongs to the disk, and not to the infalling cloud:

- the gas rotational velocity must be faster than twice the radial infall velocity, $v_{\phi} > 2v_r$,
- the gas rotational velocity must be faster than twice the vertical infall velocity, $v_{\phi} > 2v_z$,
- gas must not be thermally supported, $\frac{\rho_g v_{\phi}^2}{2} > 2P$,
- the gas number density must be higher than 10^9 cm^{-3} .

Here, v_z , v_r , and v_ϕ are the components of gas velocity in the cylindrical coordinates, ρ_g the volume density of gas, and P the gas pressure. If any of the first three conditions fails, a particular grid cell is not qualified as belonging to the disk. The forth condition must always be fulfilled. We also tried a higher threshold for the gas number density 10^{10} cm^{-3} but found little difference.

At the earliest stages of disk evolution considered in this work ($t \leq 15$ kyr after disk formation), some radial drift and vertical settling of dust towards the disk midplane may have already occurred (Bate, 2022; Lebreuilly et al., 2020; Vorobyov et al., 2024). Therefore, the gas and dust disks may not be having identical extents. Since we use the volume density and velocity of gas to identify the disk-to-envelope interface, our algorithm identifies the gas disk rather than the dust disk. We neglect this difference in the present work, as we do not expect it to be decisive at this early evolution stage. Indeed, Hsieh et al. (2024) found that the ratio of gas to dust disk radii for Class 0 objects does not deviate much from unity.

3.2 Construction of synthetic disk images in dust continuum emission

The second step is to obtain the simulated images of our model disks in millimeter wavebands. For this purpose, we employed the RADMC-3D radiative transfer tool (Dullemond et al., 2012) and postprocessed the resulting synthetic fluxes with the ALMA Observational Support Tool (ALMA OST) to account for atmospheric effects and finite interferometer resolution. The input parameters into RADMC-3D are the three-dimensional dust volume density, temperature, and dust size distributions obtained from ngFEOSAD and the output is the radiation intensity distribution at a specific wavelength. Since we modeled the earliest stages of evolution, the radiation of the central star was neglected.

In the RADMC-3D radiation transfer simulations we used the Cartesian grid with the mesh refinement option. It allows us to directly map the ngFEOSAD nested meshes onto the RADMC-3D grid layout. We considered eight inner nested meshes of ngFEOSAD, which encompass a cube with an edge size of 1100 au centered at the FHSC. Importing the dust content of the disk into RADMC-3D calculations requires specifying its density, temperature, and dust opacity. While the first two were taken directly from hydrodynamic modeling, the absorption and scattering dust opacities were obtained using the opTool (Woitke et al., 2016) for dust grains with a fixed minimum dust size of $5 \times 10^{-3} \mu\text{m}$ and a maximum dust size a_{\max} (see also Appendix 11), which value was either fixed or directly taken from our hydrodynamic simulations. In the latter case, a_{\max} is a continuous distribution and varies from computational cell to cell, which is too complex to implement in RADMC-3D. To circumvent this problem, we introduce in each cell a number of dust sub-populations, each characterized by the same minimum size $5 \times 10^{-3} \mu\text{m}$ but different maximum sizes: $a_{\max}^{\text{sub}} = 2.0 \mu\text{m}$, $10 \mu\text{m}$, $100 \mu\text{m}$, 1 mm , and 1 cm . We then retain in each cell only the sub-population whose maximum size a_{\max}^{sub} is closest to a_{\max} .

In each Monte-Carlo RADMC-3D simulation we set the number of photons to $N = 10^8$. The synthetic radiation fluxes obtained after radiation transfer simulations are then post-processed with the ALMA OST with parameters corresponding to ALMA Band 6 or Band 3. In particular, the bandwidth is set to 7.5 GHz, the beam size is varied from $0.042'' \times 0.046''$ to $0.134'' \times 0.146''$, and the on-source time is equal to 1.0 hour of observation. We consider the atmospheric conditions corresponding to precipitable water vapor of 1.796 mm, which results in a theoretical RMS-noise

of $\sigma \simeq 1.11 \times 10^{-5}$ Jy. We note that the adopted angular resolution is close to the highest limit¹, and may not be available at every ALMA cycle.

3.3 Estimates of disk masses and sizes from radiation fluxes

The final step is to derive the disk masses and sizes from the radiation fluxes obtained with RADMC-3D and postprocessed with ALMA OST as described above. For this purpose, we follow an approach usually employed when inferring the masses and sizes of dust disks from observations in (sub)-mm wavebands (e.g., Tobin et al., 2020; Kóspál et al., 2021). First, we determine the radial extent within which 90% or 97% of the total flux at a given wavelength is confined, $R_{90\%}^{\text{obs}}$ or $R_{97\%}^{\text{obs}}$. The former value is often used in observational astronomy because the low signal-to-noise ratio near the disk outer boundary may interfere with the measurements, while the latter value may be considered as an idealized upper limit that can be achieved with high signal-to-noise observations. The value of $R_{90\%}^{\text{obs}}$ is further regarded as the nominal radius of our synthetic disk, while $R_{97\%}^{\text{obs}}$ is used for comparison.

Once the radius of our synthetic disk is calculated, the dust mass of the disk is estimated using the following equation

$$M_{90\%}^{\text{obs}} = \frac{d^2 F_{\lambda}^{90\%}}{B_{\lambda}(T_{\text{d}}) \kappa_{\lambda}}, \quad (1)$$

where d is the assumed distance to the object, $F_{\lambda}^{90\%}$ is the total flux at wavelength λ contained within the disk extent defined by $R_{90\%}^{\text{obs}}$, $B_{\lambda}(T_{\text{d}})$ is the Planck function at an average dust temperature T_{d} , and κ_{λ} is the dust opacity per gram of gas. We also considered dust masses $M_{97\%}^{\text{obs}}$ contained within 97% of the total flux as an idealized limit. For the wavelength of observations we choose 1.3 mm, which corresponds to the center of the B6 band on ALMA. The dust opacity $\kappa_{\lambda=1.3 \text{ mm}}$ is set equal to $0.89 \text{ cm}^2 \text{ g}^{-1}$ for $\lambda = 1.3 \text{ mm}$ (Ossenkopf and Henning, 1994), which is a frequent observer's choice (Tobin et al., 2020; Kóspál et al., 2021), and is scaled accordingly for $\lambda = 3.0 \text{ mm}$. Details on the determination of the dust temperature T_{dust} are provided in Sect. 4.3. We note here that Equation (1) is derived in the limit of negligible dust scattering. Nevertheless, we will use in this work the synthetic fluxes and dust opacities that consider the effects of dust scattering. This is done because fluxes from real disks are by default affected by dust scattering. However, in Appendix 10 we conducted several experiments and turned off dust scattering to assess its effects on the synthetic fluxes. Equation (1) is valid for the optically thin limit, but we will apply it to disk configurations that are partly or fully optically thick for the lack of a better alternative. We note that this equation is often used in large surveys of star-forming regions and can lead to serious mass miscalculations, as we will demonstrate later in this work.

4 RESULTS

In this section, the comparison between the disk masses and sizes derived directly from hydrodynamic modeling with those derived from synthetic radiation fluxes is carried out.

¹ <https://almascience.nrao.edu/about-alma/alma-basics>

4.1 Model disk characteristics and synthetic images

Figure 1 presents the spatial distribution of the main disk characteristics in the disk midplane and at the vertical slice taken through the $x - z$ plane at $y = 0$ as obtained from numerical hydrodynamics modeling with ngFEOSAD at 15 kyr after the instance of disk formation. A clear two-armed spiral pattern is evident in both gas and dust volume density distributions in the disk midplane. The Toomre Q -parameter is less than unity in the spiral arms, indicating that the disk is strongly gravitationally unstable, but gravitational fragmentation does not yet occur (see Appendix 8 for more details). The spatial distribution of grown dust in the disk midplane mostly follows that of gas. Dust evaporation in the hot center of the FHSC is accounted for (see appendix in Das et al. (2025)). The dust size in this early stage already exceeds 1.0 mm throughout most of the disk midplane, reaching a few centimeters in the innermost regions. We note, however, that fast dust growth may be somewhat tampered by electrostatic and bouncing dust growth barriers that were not considered in our numerical model (Vorobyov et al., 2025). The spiral arms are warmer than the interspiral regions and the highest temperature is achieved in the innermost regions occupied by the FHSC.

The vertical slices reveal a radially flared gas density profile with local bulges, which correspond to the position of spiral arms. Dust settling to the disk midplane is manifested by a narrower dust density distribution than that of gas. The maximum dust size a_{\max} quickly drops with increasing vertical distance from $\sim 1 - 10$ mm in the disk midplane down to $2.0 \mu\text{m}$ at the disk-cloud interface, a value that is characteristic of the infalling cloud in our model. The temperature drops with vertical distance. This may not be realistic for evolved disks that are passively heated by the central star but is justified in our case, because the radiation input from the FHSC is expected to be insignificant and the disk is mainly heated in this stage by turbulent viscosity and PdV work, both operating more efficiently near the disk midplane, rather than in the disk atmosphere.

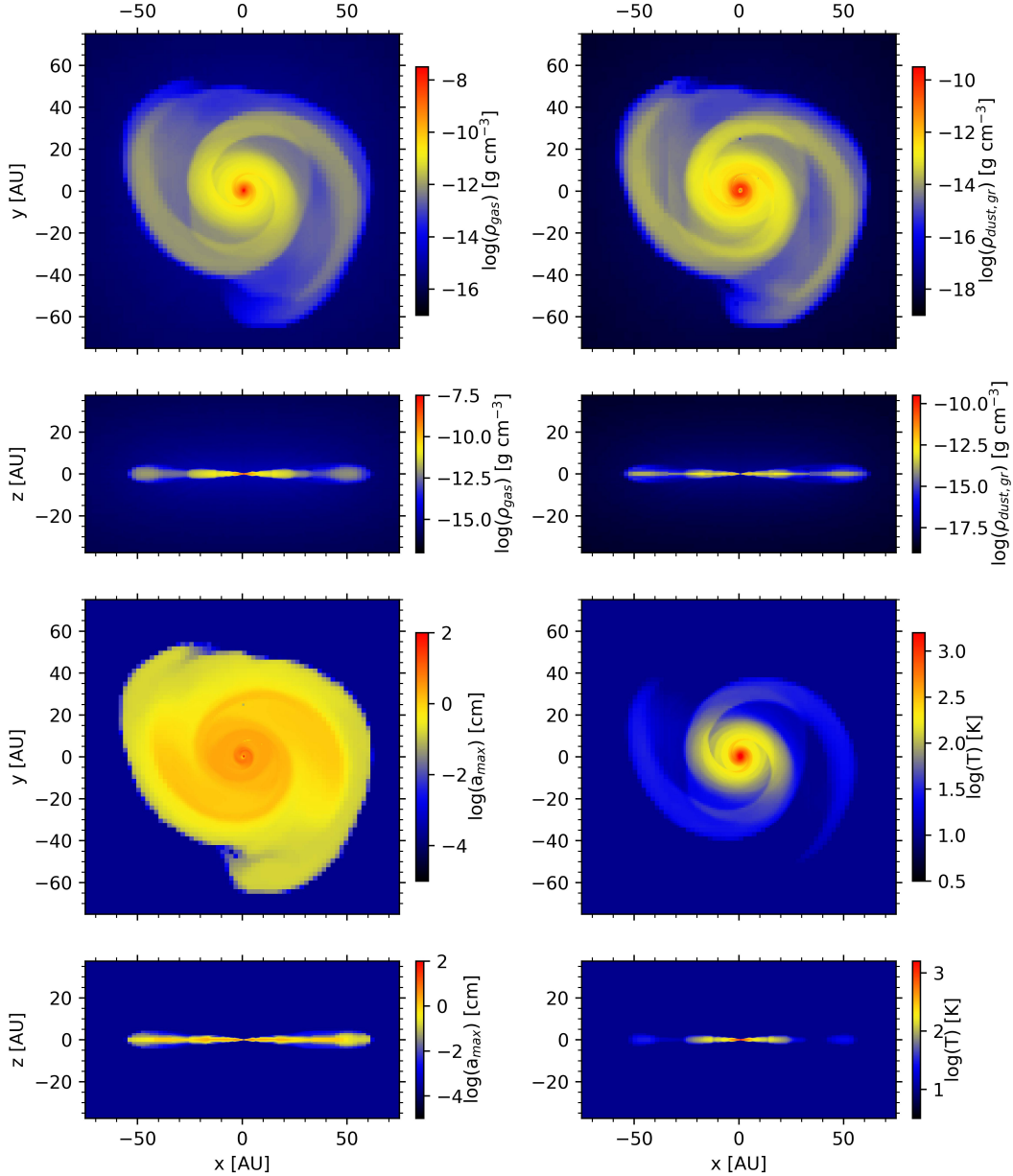


Figure 1. Model disk in the midplane and across a vertical slice. Shown are from top to bottom and from left to right: gas volume density, grown dust volume density, maximum dust size, and temperature.

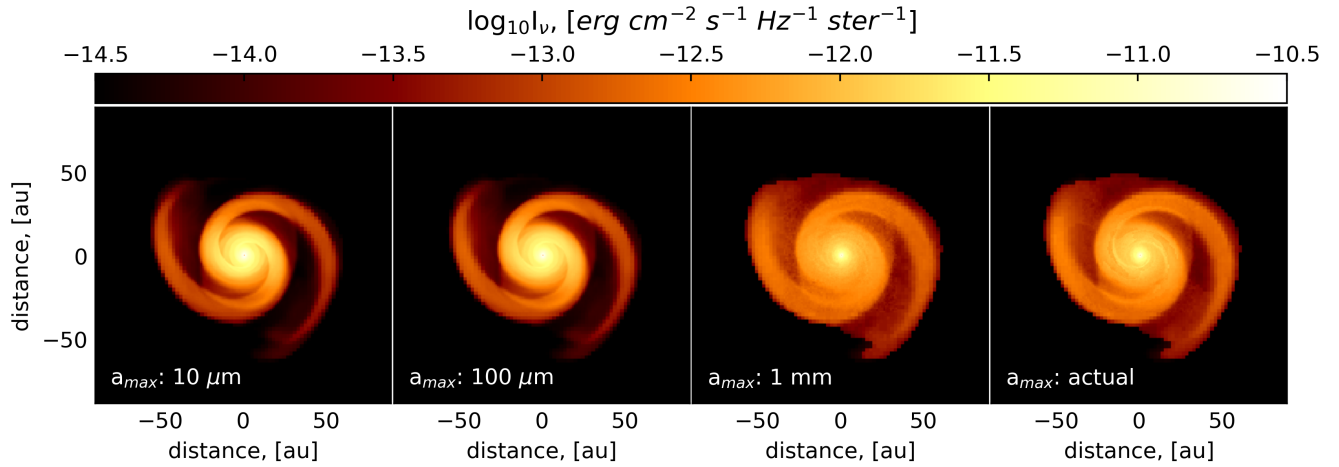


Figure 2. Synthetic intensity distributions assuming different maximum size of the dust grains in the disk. From left to right: $a_{\max} = 10 \mu\text{m}$, $100 \mu\text{m}$, 1mm , and spatially varying a_{\max} distribution, directly taken from simulations. The envelope has $a_{\max} = 2 \mu\text{m}$ in all models considered.

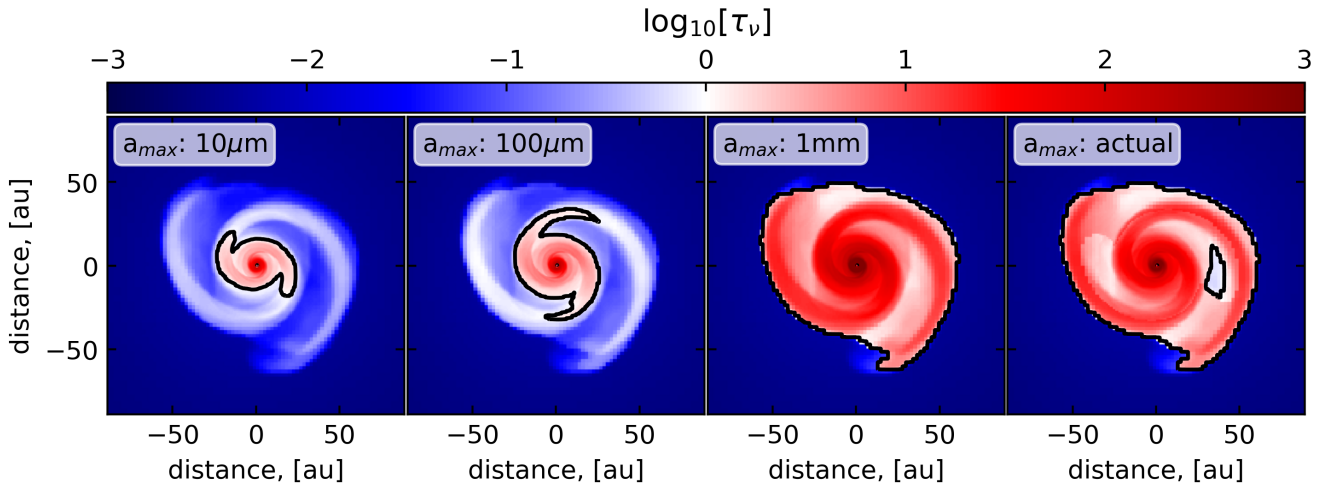


Figure 3. Optical depth in models with different maximum dust sizes in the disk. From left to right are the cases with $a_{\max} = 10 \mu\text{m}$, $a_{\max} = 100 \mu\text{m}$, $a_{\max} = 1.0 \text{ mm}$, and actual model distribution. The maximum dust size in the envelope is $2.0 \mu\text{m}$ in each case.

Figure 2 presents synthetic radiation intensity images at 1.3 mm obtained by postprocessing the model disk shown in Figure 1 with RADMC-3D. The simulation box is $1100 \times 1100 \times 1100 \text{ au}^3$, comprising the inner eight nested meshes of the entire numerical hydrodynamics domain, but we show only the inner $90 \times 90 \text{ au}^2$ region with a face-on orientation of the disk. To assess the effect of dust growth on the synthetic disk images and to account for the possible effects of electrostatic and bouncing barriers, we considered several cases of the dust size distribution across the disk. Apart from the dust size distribution directly obtained from hydrodynamic modeling with ngFEOSAD (see Figure 1) and characterized by spatially varying values of the maximum dust size a_{\max} (hereafter, referred to as “actual” distribution), we also considered several fixed values for a_{\max} . In particular, we have artificially reset the actual dust sizes throughout the disk to a constant value, keeping the

gas and dust densities unchanged. We note that we do not recompute the entire model with fixed dust sizes, but rather reset the maximum dust size alone.

Figure 2 shows the results of our experiments with a fixed $a_{\max} = 2.0 \mu\text{m}$ in the cloud, but different a_{\max} in the disk (note that the minimum size stays constant at $a_{\min} = 5 \times 10^{-3} \mu\text{m}$ in all cases). As the maximum size of dust in the disk increases, the appearance of the spiral arms in synthetic radiation intensity images becomes more diffuse. The transition is clearly evident between $a_{\max} = 100 \mu\text{m}$ and 1.0 mm. More specifically, the transition occurs between $a_{\max} = 200 \mu\text{m}$ and $300 \mu\text{m}$, but the intensity maps at these wavelengths are similar to the images at $a_{\max} = 100 \mu\text{m}$ and 1.0 mm, respectively. This effect is related to a sharp increase in the dust opacity above a certain maximum dust size, defined as $a_{\max}^{\text{crit}} = \lambda/(2\pi)$, where λ is the wavelength of observation (see Appendix 11). We note that dust of different size may also have different dynamics and efficiency of dust accumulation in spiral arms, an effect that is not considered in our controlled experiments. However, as was demonstrated in Vorobyov et al. (2024), dust trapping in spiral arms is greatly reduced due to low Stokes numbers in warm and dense environments of protoplanetary disks in the earliest evolutionary stages, an effect which is indirectly confirmed by the lack of spiral patterns in deeply embedded disks (Ohashi et al., 2023).

The effect of sharp increase in opacity is corroborated in Figure 3 showing the optical depth of our model disk at $\lambda = 1.3 \text{ mm}$ including contributions from absorption and isotropic scattering. For the case of $a_{\max}=10 \mu\text{m}$ and $100 \mu\text{m}$, the outer spiral arms and the interspiral regions are optically thin. Only the FHS, the inner disk regions and the inner parts of spiral arms are optically thick. We note, however, that these optically thick regions may contain a significant fraction of the total radiation flux (see Fig. 5). The optically thin medium effectively means that the radiation intensity is proportional to the product of the optical depth and the Planck function. For a larger $a_{\max} = 1 \text{ mm}$ and for the actual maximum dust size distribution, the optical depth is above 1.0 almost throughout the entire disk extent, apart from isolated interarmed regions, and the radiation intensity in these optically thick cases is mostly determined by the Planck function. We note also that the spiral arms appear slightly sharper when the actual dust sized distribution is applied, rather than that with a fixed upper limit of $a_{\max} = 1.0 \text{ mm}$.

4.2 Postprocessed synthetic disk images in Band 6

As a next step, we take the synthetic disk images shown in Figure 2 and postprocess them with the ALMA observational support tool (OST) (Heywood et al., 2011) to add atmospheric noise and finite resolution effects. Figure 4 depicts the resulting disk images in Band 6 of ALMA with a beam size of $0.042'' \times 0.046''$ and an exposure time of 1.0 hour. The chosen configuration provides an angular resolution that is a factor ≈ 2.3 lower than the maximum achievable resolution of ALMA in Band 6². Three different distances to the object are chosen: $R = 140 \text{ pc}$, 350 pc , and 700 pc , which correspond to the linear sizes of the beam: $\approx 6.0 \text{ au}$, 15 au , and 30 au . Varying the distance to the source but keeping the angular resolution fixed at $0.042'' \times 0.046''$ would imitate the observations of distinct star-forming clusters with the same configuration of ALMA antennas (e.g., Cycle 11, C-8). Each row of panels correspond to dust size distributions in the disk that are characterized by different maximum dust sizes a_{\max} but similar a_{\min} , both chosen in accordance with Figure 2. In the infalling cloud, the dust size spectrum is similar in all cases, with minimum and maximum dust sizes of $5 \times 10^{-3} \mu\text{m}$ and $2.0 \mu\text{m}$, respectively. We also note that in some regions beyond the

² <https://almascience.eso.org/about-alma>

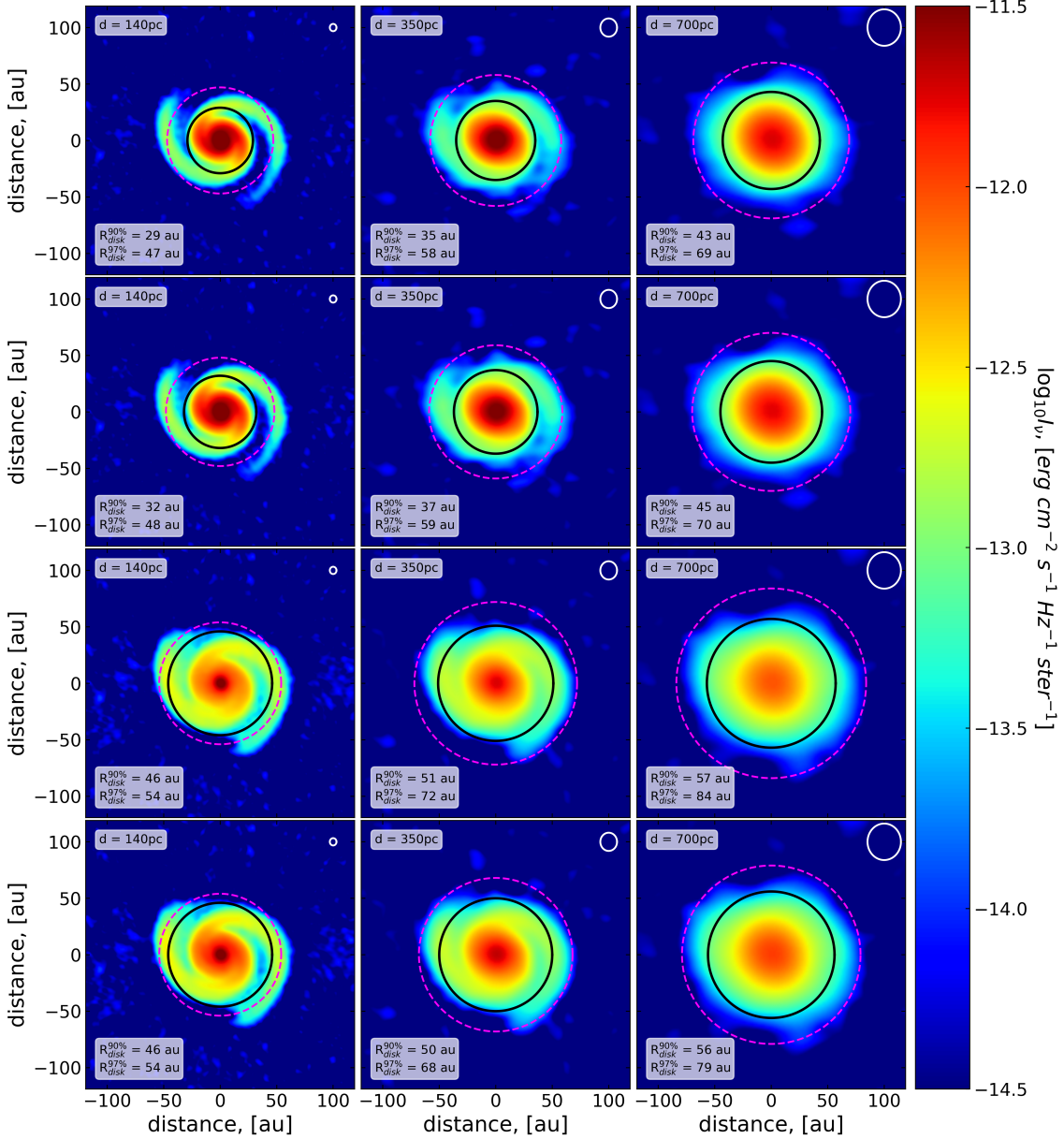


Figure 4. Synthetic intensities of the model disk at 1.3 mm obtained with RADMC-3D and postprocessed using the ALMA OST at Band 6. The three columns show, from left to right, the three assumed distances to the object: 140 pc, 350 pc, 700 pc. The rows from top to bottom are models with: $a_{\text{max}} = 10 \mu\text{m}$, $100 \mu\text{m}$, 1 mm, and actual maximal dust size in the disk. The black and red circles cover the regions of the disk where 90% and 97% of the total radiation flux is contained, defining the disk sizes according to the adopted criteria. In all cases, a_{max} in the cloud is $2.0 \mu\text{m}$. The white circles in the top-right corner of each panel show the linear size of the beam.

disk, where the detection limit was lower than noise, negative fluxes have occurred. These regions were plotted with the color corresponding the lowest detected limit, $\log I_{\nu} = -14.5$ in CGS units.

Several interesting features can be noted from our mock observations. Firstly, the spiral arms smear out with increasing distance and are visually indistinguishable at $R = 700$ pc. The spiral pattern also becomes less sharp with increasing a_{max} , as was already noted for the unprocessed radiation intensities in Figure 2. This latter finding implies that the spiral pattern caused by

gravitational instability may be easier to detect in younger disks with $a_{\max} \leq 100 \mu\text{m}$ where the main phase of dust growth is yet to occur (see also Hall et al. 2019). We also note that the fiducial criterion for the disk radius ($R_{90\%}^{\text{obs}}$) cuts out a large portion of the spiral arms in the disk if the main dust growth phase has not yet occurred (first and second rows in Fig. 4).

Secondly, the synthetic disk radii ($R_{90\%}^{\text{obs}}$ and $R_{97\%}^{\text{obs}}$) grow with increasing distance to the source. This may be the effect of beam smearing, as the linear size of the beam notably increases with distance, see the white circles in Figure 4. The effect is strongest for $a_{\max} \leq 100 \mu\text{m}$ with an increase in $R_{90\%}^{\text{obs}}$ and $R_{97\%}^{\text{obs}}$ of up to 50%, but even for the mm-cm sized grains the increase can be up to 20%. We note that subtracting about 1/2 of the linear size of the beam from the synthetic disk radii can help to compensate for the effects of beam smearing (with increasing distance) on the apparent radius of the dust disk, in particular for $R_{90\%}^{\text{obs}}$.

Thirdly, disks in a more advanced stage of dust growth look somewhat bigger. This can be related to the optical depth effects. For the case of $a_{\max} \leq 100 \mu\text{m}$, the central optically thick region of the disk ($\leq 20 \text{ au}$) dominates the radiation intensity and the optically thin spiral arms are characterized by an order of magnitude weaker values (see Fig. 4). For large grains and optically thick disks, the contrast between the inner and outer disk regions is reduced.

Indeed, Figure 5 demonstrates that the radial intensity profiles of the synthetic disk in the $a_{\max} \leq 100 \mu\text{m}$ limit are steep and fall off with distance rapidly. A substantial fraction of the integrated radiation flux is, therefore, localized within the inner compact region of the disk. For models with $a_{\max} \geq 1.0 \text{ mm}$, however, the radiation intensity has a weaker contrast between the inner disk regions and the spiral arms, both being optically thick. As a result, the radial intensity profiles become shallower, making the disk look bigger when the same criterion (90% or 97%) for the integrated radiation flux is applied. At the same time, beam smearing also makes the intensity profiles look shallower as the distance to the source increases, regardless of a_{\max} . We also note that for models with $a_{\max} \geq 1.0 \text{ mm}$ the radiation intensity in the central regions of the disk decreases as compared to models with $a_{\max} \leq 100 \mu\text{m}$. This is the effect of dust scattering (see Appendices 10 and 11), which also contributes to the overall decrease in the integrated radiation flux as discussed later in Sect. 4.3 in the context of dust masses.

The entire disk becomes optically thick in the $a_{\max} \geq 1.0 \text{ mm}$ models (see Figure 3) because the maximum dust size surpasses the critical value $a_{\max}^{\text{crit}} = \lambda/(2\pi)$. This effect is known as the opacity cliff, see also Appendix 11. As dust grows and the optical depth transits from the optically thin ($\tau_{\nu} < 1.0$) to the optically thick ($\tau_{\nu} > 1.0$) regime, the radiation intensity becomes proportional to the Planck function, rather than to the product of the Planck function and optical depth. Since both quantities decline with radius, the product of the two (optically thin limit) would produce a steeper distribution of the radiation intensity than just the Planck function (optically thick limit). As a result, the extent within which 90% (or 97%) of the flux is contained (the disk radius by our definition) becomes bigger in the optically thick case. The effect can be substantial, with an increase of more than 50% in $R_{90\%}^{\text{obs}}$ when the maximum dust sizes grows from $a_{\max}=10 \mu\text{m}$ to mm-cm sized grains in the disk. The trend is also present but less expressed when $R_{97\%}^{\text{obs}}$ is used.

4.3 Synthetic disk masses

The first step in calculating the synthetic disk masses is to determine the flux F_{λ} in Equation (1). Table 2 presents the integrated synthetic fluxes contained within $R_{90\%}^{\text{obs}}$ and $R_{97\%}^{\text{obs}}$ for all three

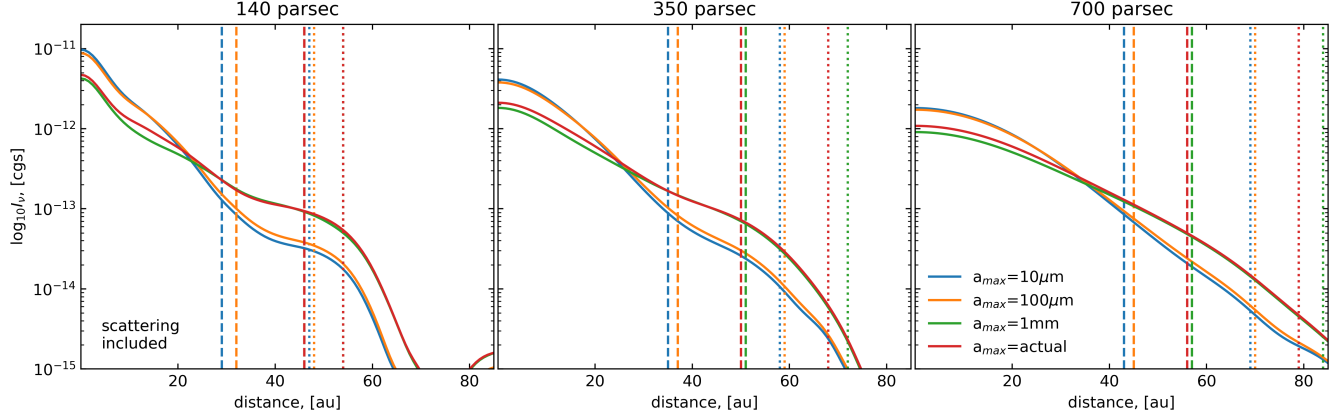


Figure 5. Radial profiles of the radiation intensity in CGS units after postprocessing with ALMA OST. The profiles are obtained by azimuthally averaging the corresponding spatial distributions shown in Fig. 4. The vertical dashed and dotted lines indicate the radial positions within which 90% or 97% of the total flux is localized, respectively. Panels from left to right correspond to different adopted distances to the source.

Table 1. Synthetic disk radii in Band 6

Dust size [a_{\max}]	$R_{90\%}^{\text{obs}}/R_{97\%}^{\text{obs}}$ [au]	$\Delta R_{90\%}^{\text{obs}}/\Delta R_{97\%}^{\text{obs}}$ [au]	$R_{90\%}^{\text{obs}}/R_{97\%}^{\text{obs}}$ [au]	$\Delta R_{90\%}^{\text{obs}}/\Delta R_{97\%}^{\text{obs}}$ [au]	$R_{90\%}^{\text{obs}}/R_{97\%}^{\text{obs}}$ [au]	$\Delta R_{90\%}^{\text{obs}}/\Delta R_{97\%}^{\text{obs}}$ [au]
10 μm	29/47	-24/-6	35/58	-18/+5	43/69	-10/+16
100 μm	32/48	-21/-5	37/59	-16/+6	45/70	-8/+31
1.0 mm	46/54	-7/+1	51/72	-2/+19	57/84	+4/+31
actual	46/54	-7/+1	50/68	-3/+15	56/79	+3/+26

Notes. Each pair of columns (from left to right) presents the synthetic disk radii and their deviations from the true value of $R_{\text{disk}}^{\text{mod}} = 53$ au for distances $d = 140$ pc, 350 pc, and 700 pc, respectively. Plus and minus signs correspond to over- and underestimates. The slash separates values obtained with different definition of the disk radius.

Table 2. Integral radiation fluxes in Band 6

Dust size [a_{\max}]	$F_{90\%}^{\text{obs}}/F_{97\%}^{\text{obs}}$ [mJy]	$F_{90\%}^{\text{obs}}/F_{97\%}^{\text{obs}}$ [mJy]	$F_{90\%}^{\text{obs}}/F_{97\%}^{\text{obs}}$ [mJy]
10 μm	347/375	57/62	14.4/15.5
100 μm	350/375	57/62	14.4/15.5
1.0 mm	265/286	45/48	11.2/12.0
actual	302/324	50/54	12.6/13.6

Notes. Second, third, and fourth columns present the fluxes at distances $d = 140$ pc, 350 pc, and 700 pc, respectively. The slash separates values obtained with different definition of the flux.

adopted distances. As expected, $F_{90\%}^{\text{obs}}$ and $F_{97\%}^{\text{obs}}$ decrease with distance, but their behavior with increasing a_{\max} is more complex. The highest values are found for $a_{\max} \leq 100 \mu\text{m}$ and the lowest are around $a_{\max} = 1.0 \text{ mm}$. The decrease in the flux at the advanced stages of dust growth is likely caused by flux dilution due to strong dust scattering at mm-sized grains, see Appendices 10 and 11.

Table 3. Synthetic dust masses in Band 6 at particular T_d

Dust size [a_{\max}]	$M_{90\%}^{\text{obs}}(T_d = 20 \text{ K})$ [M_{\oplus}]	$M_{90\%}^{\text{obs}}(T_d = 30 \text{ K})$ [M_{\oplus}]	$M_{90\%}^{\text{obs}}(T_d = 40 \text{ K})$ [M_{\oplus}]
10 μm	493.5	297.9	212.8
100 μm	497.4	300.3	214.5
1.0 mm	376.2	227.1	162.2
actual	429.1	259	185

Notes. Distance to the source is $d = 140$ pc. The intrinsic dust mass in the disk is $M_{\text{dust}}^{\text{mod}} = 673 M_{\oplus}$.

To determine dust masses from the synthetic disk images shown in Figure 4, we should also know the value of the average dust temperature T_d that enters Equation (1). This quantity is hard to constrain directly from observations and therefore the average dust temperature is often determined for young protoplanetary disks (Class 0 and I) following Tobin et al. (2020) as:

$$T_d = 43 \text{ K} \left(\frac{L_*}{1.0 L_{\odot}} \right)^{0.25}, \quad (2)$$

where L_* is the luminosity of the central source. This relation is based on radiation transfer simulations of a protoplanetary disk embedded into an envelope and heated only by the central star. This case is different from the earliest evolutionary stage considered in this study, in which the disk is actively heated by internal hydrodynamic processes and stellar irradiation is neglected. Therefore, Equation (2) is not directly applicable in our case.

We could have used the actual hydrodynamic data to derive T_d as an alternative. However, we adopted a barotropic equation of state, which is a simplification compared to the solution of the full energy balance equation including radiation transfer. We also note that the ngFEOSAD code makes no distinction between the gas and dust temperatures. More sophisticated simulations demonstrate that deviations may occur at the disk-envelope interface where a higher temperature of gas than that of dust may be expected due to heating by the shock wave caused by the infalling envelope (Pavlyuchenkov et al., 2015; Bate and Keto, 2015; Vorobyov et al., 2020).

Considering these uncertainties we decided not to focus on a particular value of the mean dust temperature but instead used a range of $T_d = 10 - 50$ K when calculating the dust mass in Equation (1). We note that Dunham et al. (2014) found that an average temperature declines from 30 K for Class 0 to 15 K for Class I objects, and an upper limit of 50 K for a very young disk considered in this work is consistent with a general temperature decline with age (Commerçon et al., 2012).

Using Equation (1), we can now calculate the dust mass contained within the synthetic disk shown in Figure 4, with its radius defined by either $R_{90\%}^{\text{obs}}$ or $R_{97\%}^{\text{obs}}$. We note that the dust opacity is that of Ossenkopf and Henning (1994) for all calculations in this section. The resulting values are plotted in Figure 6. The synthetic masses of dust vary with a_{\max} in the same manner as the integrated radiation fluxes, namely, they decrease at the advanced stages of dust growth when a_{\max} transits from 10 μm to 1.0 mm, likely due to flux dilution by scattering on grown dust grains. An opposite trend is observed when a_{\max} changes from 1.0 mm to the actual dust size distribution,

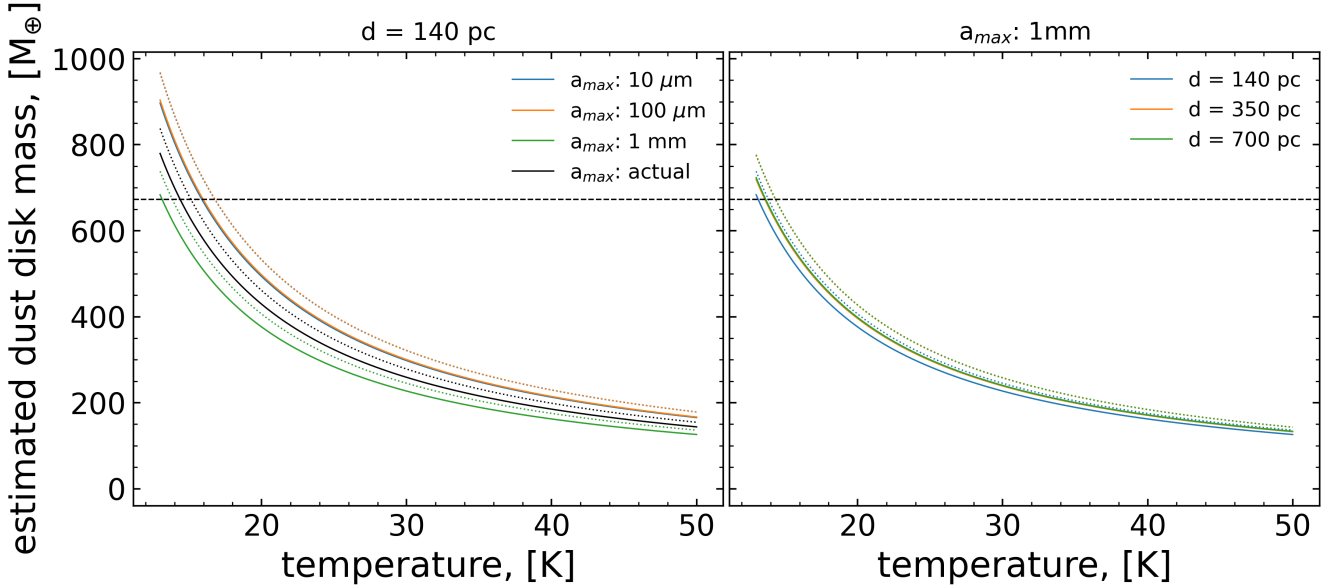


Figure 6. Masses of dust in the synthetic disk. The left column shows the masses as a function of a_{\max} but for the fixed distance to the source $d = 140$ pc, while the right column corresponds to distinct d but fixed $a_{\max} = 1.0$ mm. Solid and dotted lines represent the mass estimates using $R_{90\%}^{\text{obs}}$ and $R_{97\%}^{\text{obs}}$, respectively. The horizontal dashed line defines the intrinsic dust mass in the model disk.

which is on average higher than 1.0 mm, see Fig. 1. Interestingly, the peak in the dust scattering opacity is also located around 1.0 mm, see Fig. 16, thus reinforcing our conclusion about the effects of scattering on the dust mass estimates. At the same time, $M_{90\%}^{\text{obs}}$ and $M_{97\%}^{\text{obs}}$ only insignificantly vary with distance to the source, and this small variation is probably due to beam smearing.

We now compare the synthetic dust masses shown in Figure 6 with the actual mass of dust in our model disk. The latter is calculated by summing up all dust within the disk extent defined by the red contour line in Figure 14 (see Appendix 9). The resulting value is $M_{\text{dust}}^{\text{mod}} \approx 673 M_{\oplus}$ (evaporated dust in the FHSC is not counted), almost independent of the threshold gas number density (10^9 or 10^{10} cm^{-3}). Figure 6 demonstrates a strong dependence of the synthetic dust mass on the dust temperature. In all models considered, the dust mass is heavily underestimated for $T_d \geq 20$ K by factors of several. The mismatch is somewhat sensitive to the adopted radius of the disk: $R_{90\%}^{\text{obs}}$ or $R_{97\%}^{\text{obs}}$, or to the dust growth phase, but the trend to underestimate the intrinsic dust mass persists. For the reader's convenience, Table 3 provides the synthetic dust masses at several T_d . The underestimate of dust mass in the disk found for very young disks in our study is in agreement with similar conclusions by Dunham et al. (2014) for Class 0 and I disks, see also Sect. 5. A good match between the synthetic and intrinsic dust masses can only be achieved for $T_d < 20$ K, and in particular for $T_d = 15.9$ K, 16.0 K, 13.1 K, and 14.4 K in models with $a_{\max} = 10 \mu\text{m}$, $a_{\max} = 100 \mu\text{m}$, $a_{\max} = 1.0$ mm, and in the model with the actual dust size distribution, respectively. These values were derived using $R_{90\%}^{\text{obs}}$ as the disk radius. We emphasize that the best-fit temperatures are lower than what is usually assumed when recovering dust masses from observations, $T_d = 20 - 40$ K (Ansdell et al., 2017; Tobin et al., 2020; Kóspál et al., 2021), but are comparable to the average temperature in the envelope and the optically thin disk regions. As we will see below, the proper choice of average dust temperature may also depend on a_{\max} and the ALMA band.

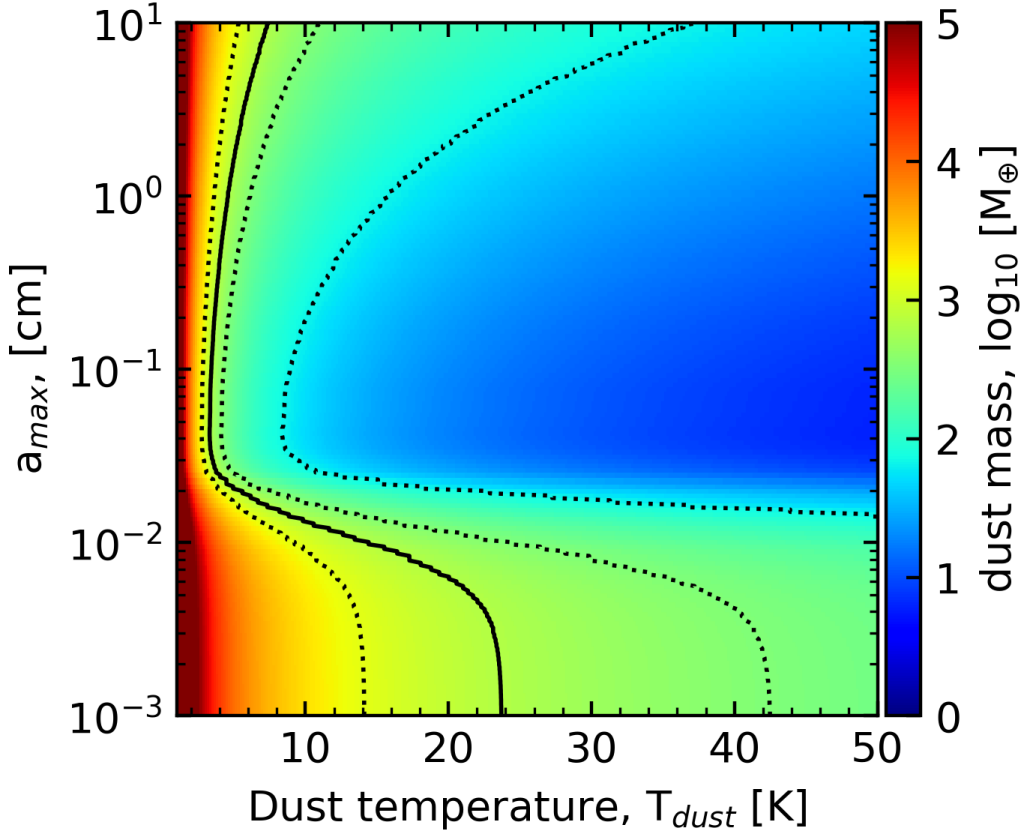


Figure 7. Synthetic dust mass in the disk, $M_{90\%}^{\text{obs}}$, as a function of dust temperature and maximum dust size. Radiation fluxes for the actual dust size distribution in Band 6 were used to derive the masses. The solid line indicates the true dust mass in the disk, $M_{\text{disk}}^{\text{mod}} = 673 M_{\oplus}$. The dotted lines delineate the synthetic dust masses that differ by factors 2.0, 0.5, 0.1 from the true disk mass.

4.4 The effect of dust-size-dependent opacities

The value of the mean dust temperature depends on the intricacies of the averaging procedure (Tobin et al., 2020) and on the disk evolutionary stage (Dunham et al., 2014; Ansdell et al., 2017), and thus may vary in wide limits. However, this may not be the only cause of mismatch between the intrinsic and synthetic disk masses. Dust opacity is known to depend on the dust size spectrum and, in particular, on the maximum dust size. Since dust growth has proven to be efficient already in the very early stages of evolution, uncertainties with the actual sizes of dust grains and, thus, with the dust opacity may also affect the dust mass estimates. Instead of using the OH5 opacity $\kappa_{\lambda=1.3 \text{ mm}} = 0.89 \text{ cm}^2 \text{ g}^{-1}$ from Ossenkopf and Henning (1994), as was done in Sect. 4.3 following the common practice in observational astronomy (Tobin et al., 2020; Kóspál et al., 2021), we now adopt the dust-size dependent absorption and scattering opacities from Woitke et al. (2016) (see Fig. 16 in Appendix 11). We note that Ossenkopf and Henning (1994) opacities are proper to use for cold dark clouds, rather than for very high-density environments of disks.

Figure 7 shows the synthetic dust masses in the disk $M_{90\%}^{\text{obs}}$, derived using Equation (1) for a wide range of dust temperatures and maximum dust sizes. To guide the eye, the black line shows the intrinsic dust mass in the disk, $M_{\text{disk}}^{\text{mod}} = 673 M_{\oplus}$. The slope of the dust size distribution is always kept equal $p = -3.5$ and the distance to the source is 140 pc.

Clearly, there is no universal dust temperature that would provide the best match between the synthetic and intrinsic dust masses in the disk if dust growth is considered and the corresponding dust-size-dependent opacities are used. The dust temperature for which both masses match ($M_{90\%}^{\text{obs}} = M_{\text{disk}}^{\text{mod}} = 673 M_{\oplus}$) for a particular dust size distribution varies from ≈ 23 K in disks with low to moderate dust growths ($a_{\text{max}} \leq 100 \mu\text{m}$) to as low as 3.0 K for disks with $a_{\text{max}} \approx 1.0 \text{ mm}$, and again increases to approx 8–20 K for disks with advanced dust growth ($a_{\text{max}} \geq 10 \text{ cm}$). Extremely low dust temperatures required to match the intrinsic dust mass around $a_{\text{max}} \approx 1.0 \text{ mm}$ are caused by the increase in dust opacity at the opacity cliff (see Fig. 16). We also note that an assumption of $T_{\text{d}} > 23$ K would always underestimate the intrinsic dust mass, regardless of the progress in dust growth, while lower temperatures may also overestimate dust mass in the limit of $a_{\text{max}} \leq 100 \mu\text{m}$.

4.5 Effects of ALMA configuration

In the previous sections, model disks located at different distances of 140 pc, 350 pc, and 700 pc but observed with a similar beam size of $0.042'' \times 0.046''$ were considered. This setup imitated distinct star-forming clusters located at different distances from the Sun but observed with the same ALMA configuration. In this section, we explore another setup and consider a model disk observed at a fixed distance of 140 pc but with different angular resolution. In particular, two beam sizes are considered: $0.042'' \times 0.046''$ and $0.134'' \times 0.146''$. The linear sizes of the beam in this case are 6 au and 16 au, respectively. This case imitates observations of the same star-forming cluster but with different ALMA configurations (e.g., Cycle 11, Configurations C-8 and C-6, respectively).

Figure 8 compares the resulting synthetic disk images. The effect of changing the beam size on the synthetic disk masses and sizes is similar to that seen in Figure 4 where the beam size was fixed but distance to the source was changing. In particular, the synthetic disk radius grows with increasing beam size by about 10%, likely due to the effect of beam smearing, while the dust mass is only slightly affected and increases by less than 1%. It seems that the beam smearing insignificantly alters the total flux, which determines the dust mass estimates (see Eq. 1). Although the disk radius increases, this effect has little consequence for the mass estimates because the radiation intensity rapidly declines with radial distance near the disk outer edge (see, Fig. 5). We also note that the spiral pattern is significantly smoothed out and barely visible for a beam size of $0.134'' \times 0.146''$, even for the closest possible distance of 140 pc.

4.6 Other ALMA bands

In this section, we show synthetic observations of the disk at the ALMA Band 3 ($\lambda = 3.0 \text{ mm}$) for comparison. The beam size in this case is set equal to $0.105'' \times 0.115''$ and the corresponding configuration provides an angular resolution that is a factor ≈ 2.5 lower than the maximum achievable resolution in Band 3. The linear sizes of the beam at the adopted distances of 140 pc, 350 pc, and 700 pc are $\approx 15 \text{ au}$, 38 au , and 75 au . Dust opacities in Ossenkopf and Henning (1994) were tabulated only out to $\lambda = 1.3 \text{ mm}$. For consistency, we extrapolate the opacity to longer wavelengths using the following relation

$$\kappa_{\lambda=3.0 \text{ mm}} = \kappa_{\lambda=1.3 \text{ mm}} \left(\frac{\lambda = 1.3 \text{ mm}}{\lambda = 3.0 \text{ mm}} \right)^{\beta}, \quad (3)$$

where the dust opacity index is set equal to $\beta = 1.8$ as in Ossenkopf and Henning (1994).

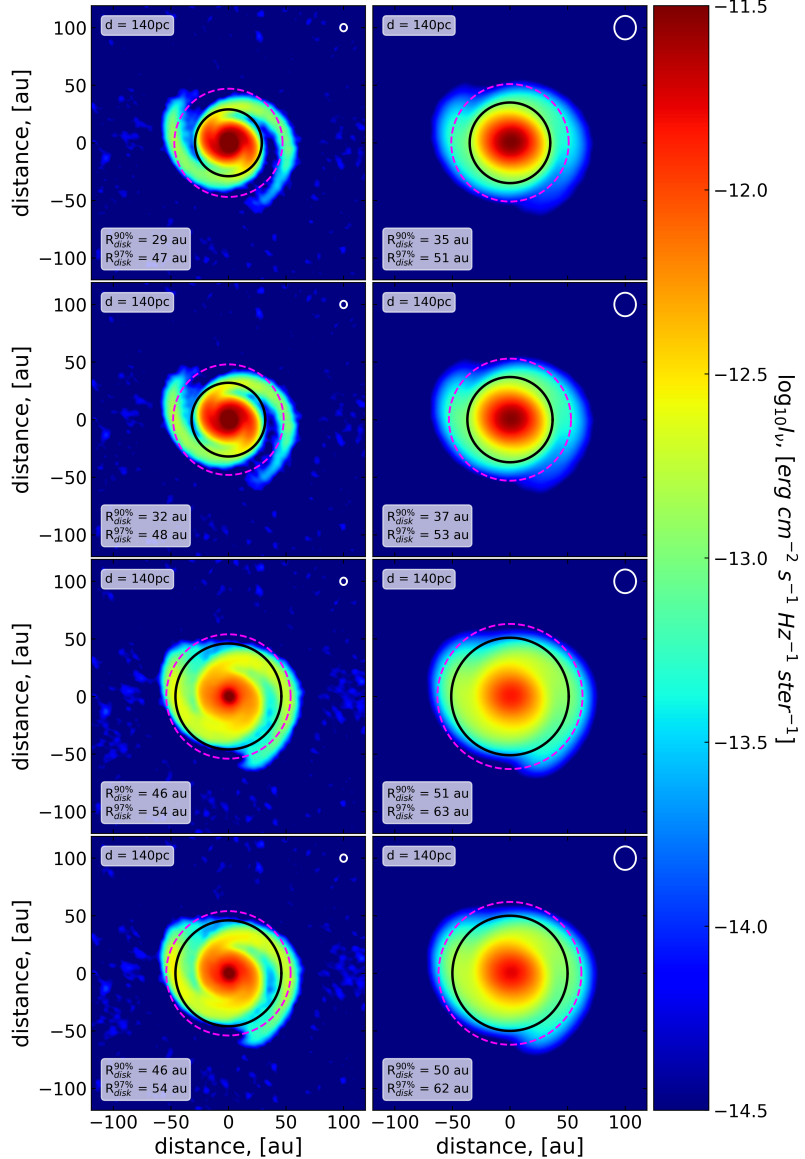


Figure 8. Synthetic intensity distribution of the model disk at 1.3 mm postprocessed using the ALMA OST for Band 6. The two columns show the effects of different beam sizes: $0.042'' \times 0.046''$ (left) and $0.134'' \times 0.146''$ (right). The distance to the object is 140 pc in both cases. The models shown from top to bottom: $a_{\max}^{\text{disk}} = 10 \mu\text{m}$, $100 \mu\text{m}$, 1 mm , and variable maximal size in the disk. The black and red circles cover the regions of the disk where 90% and 97% of the total flux is contained. The linear size of the beam is indicated with white circles.

Figure 9 presents the resulting synthetic images. The radiation intensity in Band 3 notably decreases compared to Band 6, as expected for a longer wavelength. At the same time, the integrated flux increases with growing a_{\max} as Table 4 demonstrates, unlike Band 6 where we saw the opposite trend caused by flux dilution due to a sharp increase in dust scattering around $a_{\max} = 1.0 \text{ mm}$. Apparently, the increase of radiation flux due to transition from the optically thin regime to the optically thick one (see Fig. 11 below) outweighs the effect of dust scattering in Band 3.

We find that the synthetic disk radius increases with distance somewhat stronger than in the case of Band 6. This can be expected, as the linear sizes of the beam in Band 3 are greater than

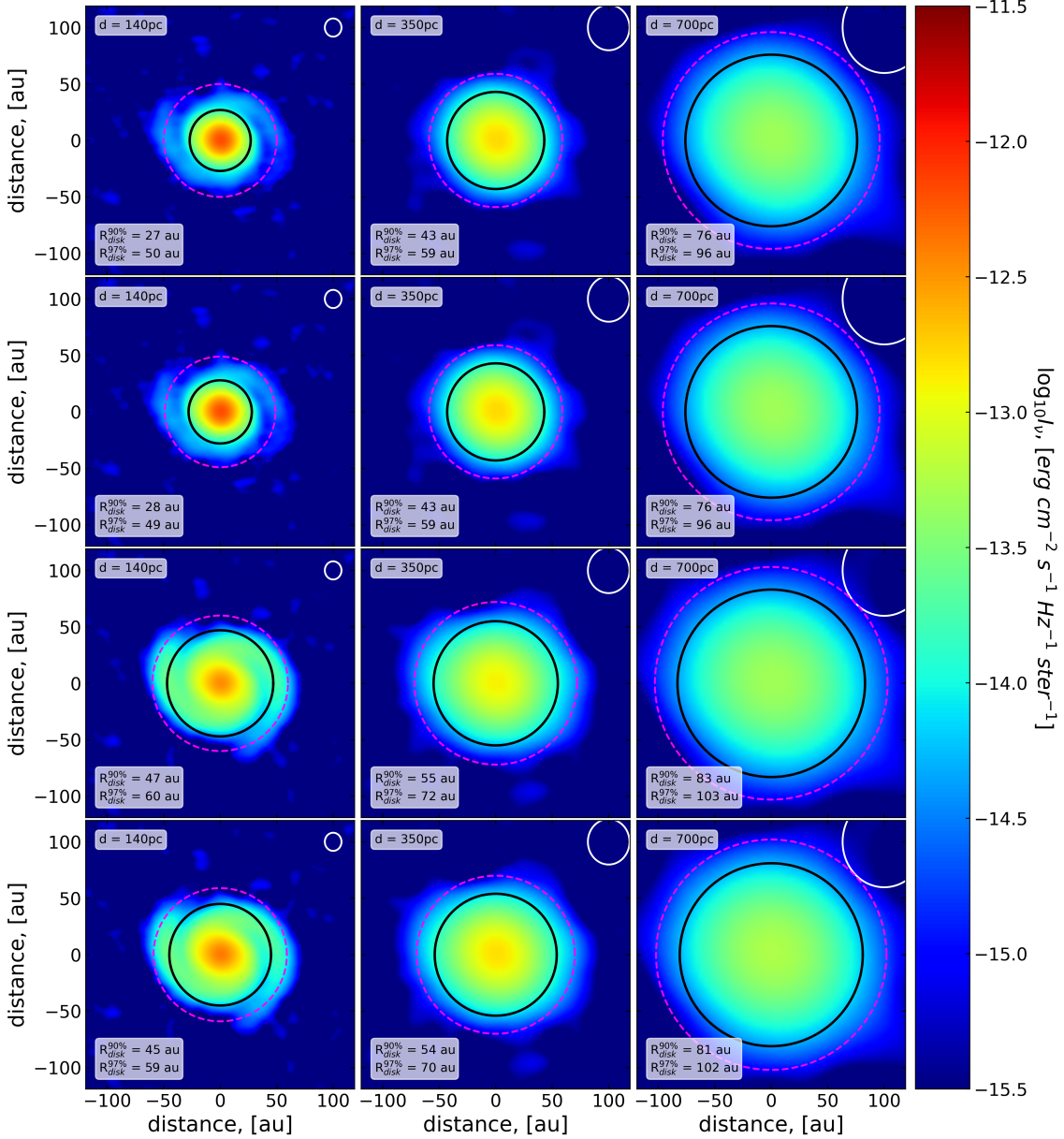


Figure 9. Similar to Fig. 4 but for Band 3 with a beam size of $0.105'' \times 0.115''$.

for the case of Band 6 (the latter is generally characterized by higher resolution) and the effect of beam smearing in Band 3 is stronger. The increase in $R_{90\%}^{\text{obs}}$ and $R_{97\%}^{\text{obs}}$ can be as large as 70% for $a_{\text{max}} \leq 100 \mu\text{m}$ and about 90% for bigger grains. We also see an increase in the synthetic disk radius as dust grows. The effect is more pronounced for smaller linear sizes of the beam (better resolution) where the effect of beam smearing is not dominant. The resulting synthetic disk radii are provided in Table 6. We note here that the disk is marginally resolved at 350 pc and is not resolved at 700 pc, thus the corresponding disk size estimates must be taken with care.

The synthetic dust masses are shown in Figure 10 for a range of T_{d} and Ossenkopf and Henning (1994) opacity. A good agreement with the intrinsic dust mass is achieved for $T_{\text{d}} = 30.9 \text{ K}$, 31.6 K , 36.8 K and 41.4 K in models with $a_{\text{max}} = 10 \mu\text{m}$, $100 \mu\text{m}$, 1.0 mm and in the model with the actual dust size distribution, respectively. All estimates adopt $R_{90\%}^{\text{obs}}$ as the disk radius. These best-fit T_{d}

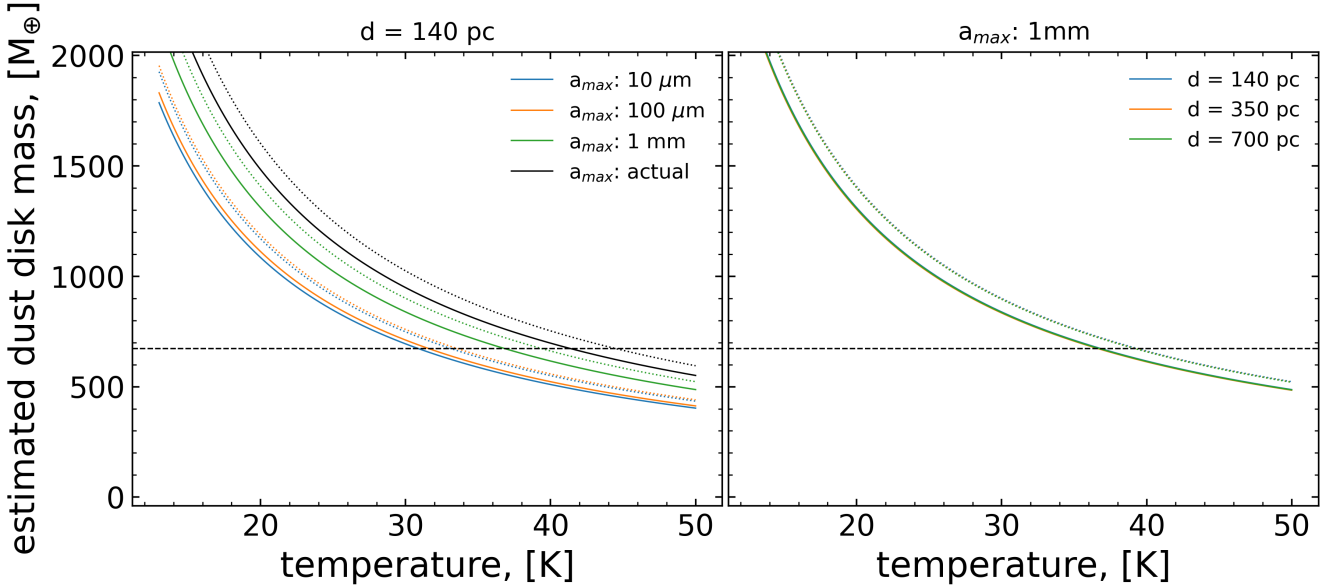


Figure 10. Similar to Fig. ?? but for Band 3.

Table 4. Integral radiation fluxes in Band 3

Dust size [a_{\max}]	$F_{90\%}^{\text{obs}}/F_{97\%}^{\text{obs}}$ [mJy]	$F_{90\%}^{\text{obs}}/F_{97\%}^{\text{obs}}$ [mJy]	$F_{90\%}^{\text{obs}}/F_{97\%}^{\text{obs}}$ [mJy]
10 μm	37.6/40.6	6.02/6.47	1.50/1.62
100 μm	38.5/41.1	6.11/6.57	1.53/1.64
1.0 mm	45.4/48.8	7.23/7.78	1.81/1.94
actual	51.4/55.5	8.25/8.84	2.05/2.21

Notes. Similar to Table 2, but for Band 3.

are within the range of average dust temperatures adopted in observational studies (Ansdell et al., 2017; Tobin et al., 2020; Kóspál et al., 2021). This means that the dust mass estimates in Band 3 are expected to be more accurate than in Band 6, although notable deviations, both underestimates and overestimates, are possible as T_d varies in the 20–50 K limits. In general, the best-fit T_d increases at the advanced stages of dust growth. As was the case for Band 6, the synthetic disk masses weakly depend on the distance to the source. The resulting synthetic disk masses for several T_d are provided in Table 5.

The reason for a better recovery of the intrinsic dust mass is in the systematically lower optical depths of the disk in Band 3. Figure 11 shows the optical depth in Band 3 for models with different maximum dust sizes a_{\max} , considering both dust absorption and scattering. For models at the initial stages of dust growth ($a_{\max} \leq 100 \mu\text{m}$), the disk is mostly optically thin, apart from the very inner region with a size of several astronomical units. For advanced stages of dust growth ($a_{\max} \geq 1.0 \text{ mm}$), the bulk of the disk is optically thick, but on average τ_{ν} is a factor of several lower than for the Band 6 case (see Fig. 3).

Figure 12 shows the effects of dust growth and varying dust temperature on dust mass estimates. Now, we use the dust-size-dependent opacities (rather than those of Ossenkopf and Henning 1994) to calculate the dust mass using Equation (1). As for the case of Band 6, there is no universal dust

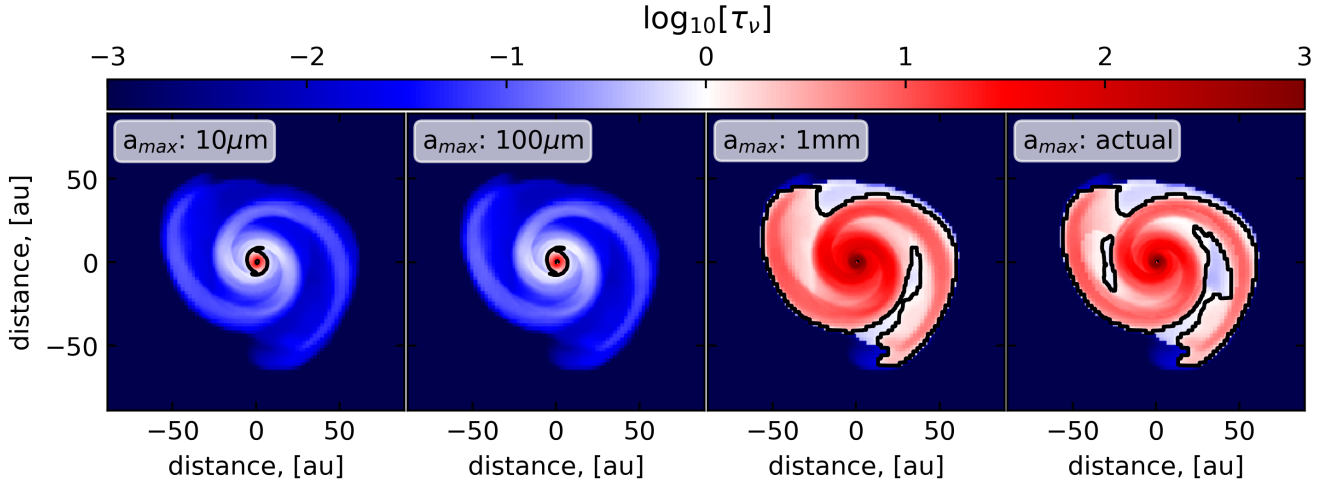


Figure 11. Similar to Fig. 3 but for Band 3.

Table 5. Synthetic dust masses in Band 3 for particular T_d

Dust size [a_{\max}]	$M_{90\%}^{\text{obs}}(T_d = 20 \text{ K})$ [M_{\oplus}]	$M_{90\%}^{\text{obs}}(T_d = 30 \text{ K})$ [M_{\oplus}]	$M_{90\%}^{\text{obs}}(T_d = 40 \text{ K})$ [M_{\oplus}]
10 μm	1085	694	510
100 μm	1112	711	522
1.0 mm	1311	839	616
actual	1483	949	697

Notes. Distance to the source is $d = 140$ pc. The intrinsic dust mass in the disk is $M_{\text{dust}}^{\text{mod}} = 673 M_{\oplus}$.

Table 6. Synthetic disk radii

Dust size [a_{\max}]	$R_{90\%}^{\text{obs}}/R_{97\%}^{\text{obs}}$ [au]	$\Delta R_{90\%}^{\text{obs}}/\Delta R_{97\%}^{\text{obs}}$ [au]	$R_{90\%}^{\text{obs}}/R_{97\%}^{\text{obs}}$ [au]	$\Delta R_{90\%}^{\text{obs}}/\Delta R_{97\%}^{\text{obs}}$ [au]	$R_{90\%}^{\text{obs}}/R_{97\%}^{\text{obs}}$ [au]	$\Delta R_{90\%}^{\text{obs}}/\Delta R_{97\%}^{\text{obs}}$ [au]
10 μm	27/50	-26/-3	43/59	-10/+6	76/96	+23/+43
100 μm	28/49	-25/-4	43/59	-10/+6	76/96	+23/+43
1.0 mm	47/60	-6/+7	55/72	+2/+19	83/103	+30/+50
actual	45/50	-8/+7	54/70	+1/+17	81/102	+28/+49

Notes. Similar to Table 1 but for Band 3

temperature that can provide a good match between synthetic and intrinsic dust masses in the disk when dust growth is considered. For the initial stages of dust growth, when $a_{\max} \leq$ a few $\times 100 \mu\text{m}$, any choice of T_d below 50 K overestimates the true dust mass. At larger a_{\max} , the dust mass is in general underestimated, unless for very small $T_{\text{dust}} < 10 \text{ K}$.

We also note that the spiral structure is only detectable at a distance of 140 pc and is completely smoothed out at larger distances, unlike Band 6 for which the spiral structure was still visible at a distance of 350 pc (see Fig. 4). The $R_{90\%}^{\text{obs}}$ circle cuts out a large fraction of the spiral arms for models with $a_{\max} \leq 100 \mu\text{m}$, as was also the case for Band 6.

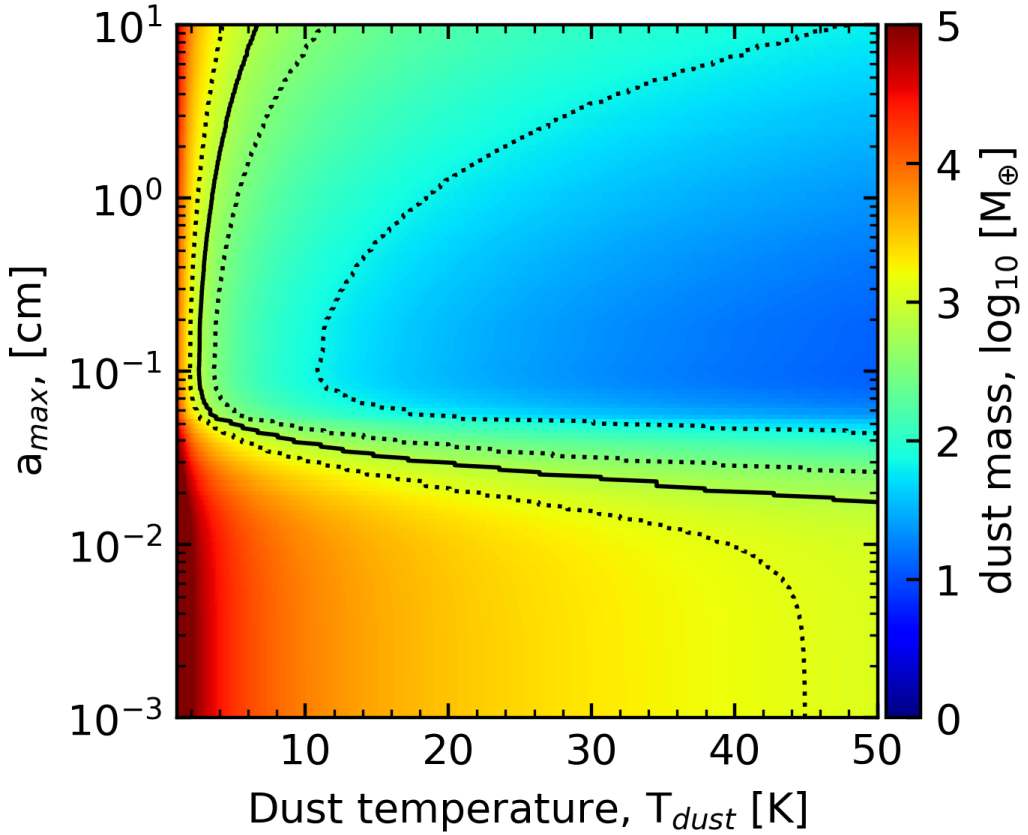


Figure 12. Similar to Fig. 12 but for Band 3.

5 DISCUSSION

This work is focused on the earliest stages of disk evolution, when the FHSC or the protostar has not yet provided sufficient luminosity output to start dominating the energy balance in the disk and the disk temperature is instead set by internal hydrodynamic processes. This makes the radiative transfer simulations somewhat easier as there is no uncertainty with the intrinsic parameters of the growing star (such as the effective temperature and stellar radius) and the stellar luminosity output such as accretion luminosity. At the same time, this stage is short and is observationally difficult to capture. There are very few FHSC candidates (Chen et al., 2010; Pezzuto et al., 2012; Duan et al., 2023), and none have been reliably verified to date. Nevertheless, we think that it is important to explore these earliest stages, even though this study may currently represent only a theoretical prospective. In a follow-up study, we will explore subsequent Class 0 and I stages of disk evolution, where the protostar significantly contributes to the disk energy balance, with a similar numerical setup of ngFEOSAD. The current proof-of-concept theoretical work provides an important bridge to more observationally motivated studies of the Class 0 and I stages, including the disk inclination effects which were omitted in the present work.

We found that that similar disks but located in distinct star-forming regions at different distances from the Sun can have different apparent disk radii and the variation around the intrinsic value may be substantial, up to a factor of two, depending on the dust growth stage in the disk. When using the Ossenkopf and Henning (1994) opacities and dust temperatures typical for Class 0 and I disks,

Equation (1) can yield significant dust mass underestimates by factors of several. The problem is more severe in Band 6 than in Band 3 of ALMA. In the latter case, the dust mass can actually be even overestimated. We also demonstrated that by adjusting the rather uncertain dust temperature in Equation (1), it becomes possible to recover the intrinsic mass of dust in the disk. The best-fit values of T_d strongly depend on the ALMA band, but are weakly sensitive to the distance to the source.

The situation becomes more complicated when the dust-size-dependent opacities are considered. The best-fit T_d begin to strongly depend on a_{\max} , that is, on the dust growth stage in the disk. A good match between the synthetic and intrinsic dust masses for $a_{\max} \geq 1.0$ mm may require a dust temperature that is much lower than usually adopted in observational studies. We note that the best-fit T_d also depends on a_{\max} via the corresponding variations in the integrated radiation flux (see Tables 2 and 4), but the dependence via the varying dust opacity is stronger. We also note that the intricate relation between T_d and a_{\max} implies some dependence of the former on the latter. This is possible considering that T_d depends on dust opacity and dust opacity in turn depends on a_{\max} . In addition, the gas-to-dust energy transfer rate depends on the dust properties, such as the total surface area which changes as dust grows, but these effects are beyond the present study.

Our model and synthetic disk radii (see Table 1) are broadly consistent with those inferred for Class 0 disks by the CAMPOS and VANDAM surveys of the Aquila, Corona Australis, Ophiuchus North, Ophiuchus, Orion, and Serpens molecular clouds (Tobin et al., 2020; Hsieh et al., 2024). Our model, however, considers the disk at the FHSC to protostellar transition and may not be representative in terms of disk mass and radius due to short duration of this phase. In any case, the comparison of the synthetic disk radii and masses with the observationally derived samples was not the purpose of this study. Here, we explored the accuracy of inferring the true disk radii and masses from synthetic millimeter fluxes, excluding the associated uncertainties with the luminosity of the growing star but taking dust growth into consideration.

The mismatch between intrinsic and synthetic disk masses was also reported by Dunham et al. (2014) in the context of Class 0 and I disks, though without considering the effects of dust growth. It was also found that the disk masses may be underestimated by up to factors of 2–3 at millimeter wavelengths and up to an order of magnitude at sub-mm wavelengths, in particular, due to uncertainties in the optical depth and dust temperatures, as was also found in our study. In contrast, Harsono et al. (2015) found that disk masses inferred from synthetic observations in millimeter wavelength agree rather well with the actual disk masses of young embedded disks obtained from magnetohydrodynamics simulations. However, the adopted beam size of 5–15'' may have encompassed the large-scale emission of the surrounding envelope, rather than the disk itself. They also retrieved the disk mass from the total envelope+disk flux (eqs. 1-3 in Jørgensen et al. 2009). Mass underestimates of gravitationally unstable disks by factors 2.5–30 using synthetic (sub)-mm observations at different ALMA bands was also reported in Evans et al. (2017). In a more recent study by Liu et al. (2022), focused rather on Class II analytic disk models but with sophisticated dust composition and considering dust growth, possible severe underestimation of dust mass was also reported. The requirement of multi-wavelength observations for more accurate measurements of usually underestimated dust masses was also reported in Viscardi et al. (2025). We also note that multi-wavelengths observations of polarized dust emission can help to distinguish between small grains with $a_{\max} \leq 100$ μm and larger grains with $a_{\max} \sim 1.0$ mm (e.g., Guillet et al., 2020), thanks to the change in the direction of polarization from perpendicular to parallel with respect to

magnetic field lines. Interestingly, this is about a dust size range where a qualitative transition in the synthetic disk images occurs in our model (see Figs. 3 and 4). To conclude, most theoretical studies report a substantial underestimate of the dust mass when using the conventional techniques (see Eq. 1), and this issue may be inherent to all stages of disk evolution, including the very earliest considered in this work.

We finally note that the magnetic field and turbulence can have significant impacts on disk masses and sizes, especially in disk's early stages of evolution (Seifried et al., 2012; Santos-Lima et al., 2013; Lam et al., 2019; Maury et al., 2022). For instance, magnetic braking and magnetic disk winds can reduce the disk mass and size, and magnetohydrodynamic instabilities can shape the infalling envelope into streamers instead of axially symmetric infall (Machida and Basu, 2025). While the peculiar structure of the infalling envelope is unlikely to affect the synthetic images at mm-wavelengths because of its rarefied nature, a reduced disk mass could also result in lower optical depths, and, as a consequence, in more accurate mass estimates via Eq. (1). This effect can be mimicked by our collapse simulations with lower initial cloud core masses, which we leave for future studies.

6 CONCLUSIONS

In this work, we investigated the accuracy with which the mass and radius of a young protoplanetary disk can be inferred using its dust thermal emission at millimeter wavelengths. We started with a three-dimensional hydrodynamic simulation of protoplanetary disk formation with the ngFEOSAD code. We then exported the resulting density and temperature distributions of dust in the disk and envelope into the RADMC-3D code, using either the realistic dust size distribution derived directly from hydrodynamic simulations, or making simplifying assumptions about the maximum dust size to explore the possible effects of dust growth. Next, we postprocessed the radiation fluxes with the ALMA observational support tool to generate realistic synthetic images of our model disk at different ALMA bands and with different resolution. These images were finally used to calculate the synthetic disk radii and the dust masses contained with these radii using the conventional method (see Eq. 1) adopted in observational astronomy.

Four models with the maximum dust size corresponding to moderate and advanced stages of dust growth were considered: $a_{\max} = 10 \mu\text{m}$, $a_{\max} = 100 \mu\text{m}$, $a_{\max} = 1.0 \text{ mm}$, and the model with the spatially varying distribution of a_{\max} obtained from hydrodynamic simulations. We focused on a very young protoplanetary disk that formed in our simulations around a first hydrostatic core, just before it transits to a protostar. This allowed us to exclude uncertainties with the protostellar radiation output and focus on other parameters that may influence the disk mass and radius measurements. The main findings can be summarized as follows.

- When choosing the Ossenkopf and Henning (1994) opacity, dust mass can be underestimated by factors of 1.4 – 4.2 in Band 6 for the mean dust temperatures $T_d = 20 – 40 \text{ K}$, a typical range adopted in observational studies. A good match between the synthetic and intrinsic dust masses in Band 6 can be recovered for dust temperatures $T_{\text{dust}} = 13 – 16 \text{ K}$. Observations in Band 3 can both underestimate or overestimate the dust mass by up to a factor of two depending on the choice of T_d . The best-fit T_d lie in the 31–41 K limits. Synthetic disk masses in ALMA Bands 3 and 6 seem to be weakly sensitive to the distance to the source.

- When more realistic dust-size-dependent opacities are considered (see Fig. 16), the discrepancy between the synthetic and intrinsic dust masses begins to strongly depend on the maximum dust size, in addition to strong dependence on T_d . To achieve a fair agreement, information on the maximum dust size in the disk is desirable, and extremely low values of dust temperature may be required to reconcile the synthetic and intrinsic masses for $a_{\max} \geq 1.0$ mm.
- Synthetic disks look bigger at the advanced stages of dust growth $a_{\max} \geq 1.0$ mm. This may be due to the fact that most of the disk becomes optically thick as dust grows and the dust opacity reaches a peak value near $\lambda = a_{\max}/(2\pi)$.
- Synthetic disk sizes grow with increasing distance to the source and deteriorating linear resolution, likely due to the effect of beam smearing.
- Dust scattering becomes significant at the advanced stages of dust growth ($a_{\max} \simeq 1.0$ mm), affecting the radial intensity profiles and dust mass estimates, in particular in Band 6.
- Spiral pattern generated by gravitational instability is easier detected at the early stages of dust growth ($a_{\max} \leq 100$ μ m) than at the advanced stages ($a_{\max} \geq 1.0$ mm) and in Band 6 rather than in Band 3.

Both adopted definitions for the disk radius, 90% or 97% of the total flux, can either underestimate or overestimate the intrinsic disk radius, depending on the linear resolution of observations and maximum dust size. This means that a young protoplanetary disk viewed at different resolution and at different stages of dust growth would have different apparent disk radii, and the variation around the intrinsic value can be substantial, up to a factor of two. The effect of beam smearing with increasing distance can be offset by subtracting about 1/2 of the linear size of the beam from the synthetic disk radii. This work provides an important bridge to more observationally accessible Class 0 and I stages of disk evolution. In a follow-up study, we plan to use the developed algorithm to study the accuracy with which Class 0 and I disk masses and sizes can be recovered using thermal dust emission.

CONFLICT OF INTEREST STATEMENT

The authors declare that the research was conducted in the absence of any commercial or financial relationships that could be construed as a potential conflict of interest.

AUTHOR CONTRIBUTIONS

E.I.V suggested the main contents of the paper, performed ngFEOSAD simulations and wrote the paper. A.M.S. performed RADMC-3D simulations and prepared most figures. V.G.E. calculated the disk masses and radii from hydrodynamic simulations. M.D. and M.G. provided valuable inputs to the interpretations of synthetic disk models.

FUNDING

This work was supported by the Austrian Science Fund (FWF), project I4311-N27, DOI:10.55776/I4311. A.M.S. and V.G.E. also acknowledge support by the Ministry of Science and Higher Education of the Russian Federation (State assignment in the field of scientific activity 2023, GZ0110/23-10-IF).

ACKNOWLEDGMENTS

We are thankful to the anonymous referees for constructive comments that helped to improve the manuscript. Simulations were performed on the Austrian Scientific Cluster (<https://asc.ac.at/>)

DATA AVAILABILITY STATEMENT

All data related to this study can be provided on reasonable request.

REFERENCES

Anderson, A. R., Williams, J. P., van der Marel, N., Law, C. J., Ricci, L., Tobin, J. J., et al. (2022). Protostellar and Protoplanetary Disk Masses in the Serpens Region. *ApJ* 938, 55. doi:10.3847/1538-4357/ac8ff0

Ansdell, M., Williams, J. P., Manara, C. F., Miotello, A., Facchini, S., van der Marel, N., et al. (2017). An ALMA Survey of Protoplanetary Disks in the σ Orionis Cluster. *AJ* 153, 240. doi:10.3847/1538-3881/aa69c0

Ansdell, M., Williams, J. P., Trapman, L., van Terwisga, S. E., Facchini, S., Manara, C. F., et al. (2018). ALMA Survey of Lupus Protoplanetary Disks. II. Gas Disk Radii. *ApJ* 859, 21. doi:10.3847/1538-4357/aab890

Bate, M. R. (2022). Dust coagulation during the early stages of star formation: molecular cloud collapse and first hydrostatic core evolution. *MNRAS* 514, 2145–2161. doi:10.1093/mnras/stac1391

Bate, M. R. and Keto, E. R. (2015). Combining radiative transfer and diffuse interstellar medium physics to model star formation. *MNRAS* 449, 2643–2667. doi:10.1093/mnras/stv451

Bergin, E. A. and Williams, J. P. (2017). The Determination of Protoplanetary Disk Masses. In *Formation, Evolution, and Dynamics of Young Solar Systems*, eds. M. Pessah and O. Gressel. vol. 445 of *Astrophysics and Space Science Library*, 1. doi:10.1007/978-3-319-60609-5_1

Birnstiel, T., Fang, M., and Johansen, A. (2016). Dust Evolution and the Formation of Planetesimals. *SSR* 205, 41–75. doi:10.1007/s11214-016-0256-1

Birnstiel, T., Klahr, H., and Ercolano, B. (2012). A simple model for the evolution of the dust population in protoplanetary disks. *A&A* 539, A148. doi:10.1051/0004-6361/201118136

Blum, J. (2018). Dust Evolution in Protoplanetary Discs and the Formation of Planetesimals. What Have We Learned from Laboratory Experiments? *SSR* 214, 52. doi:10.1007/s11214-018-0486-5

Boss, A. P. and Kanodia, S. (2023). Forming Gas Giants around a Range of Protostellar M-dwarfs by Gas Disk Gravitational Instability. *ApJ* 956, 4. doi:10.3847/1538-4357/acf373

Chen, X., Arce, H. G., Zhang, Q., Bourke, T. L., Launhardt, R., Schmalzl, M., et al. (2010). L1448 IRS2E: A Candidate First Hydrostatic Core. *ApJ* 715, 1344–1351. doi:10.1088/0004-637X/715/2/1344

Commerçon, B., Launhardt, R., Dullemond, C., and Henning, T. (2012). Synthetic observations of first hydrostatic cores in collapsing low-mass dense cores. I. Spectral energy distributions and evolutionary sequence. *A&A* 545, A98. doi:10.1051/0004-6361/201118706

Das, I., Vorobyov, E., and Basu, S. (2025). Accretion Bursts in Young Intermediate-mass Stars Make Planet Formation Challenging. *ApJ* 983, 163. doi:10.3847/1538-4357/adb8ee

Duan, H.-Y., Lai, S.-P., Hirano, N., and Thieme, T. J. (2023). Modeling Two First Hydrostatic Core Candidates Barnard 1b-N and 1b-S. *ApJ* 947, 48. doi:10.3847/1538-4357/acb531

[Dataset] Dullemond, C. P., Juhasz, A., Pohl, A., Sereshti, F., Shetty, R., Peters, T., et al. (2012). RADMC-3D: A multi-purpose radiative transfer tool. *Astrophysics Source Code Library*, record ascl:1202.015

Dunham, M. M., Evans, N. J., Bourke, T. L., Myers, P. C., Huard, T. L., and Stutz, A. M. (2010). The Spitzer c2d Survey of Nearby Dense Cores. IX. Discovery of a Very Low Luminosity Object Driving a Molecular Outflow in the Dense Core L673-7. *ApJ* 721, 995–1013. doi:10.1088/0004-637X/721/2/995

Dunham, M. M., Vorobyov, E. I., and Arce, H. G. (2014). On the reliability of protostellar disc mass measurements and the existence of fragmenting discs. *MNRAS* 444, 887–901. doi:10.1093/mnras/stu1511

Evans, M. G., Ilee, J. D., Hartquist, T. W., Caselli, P., Szűcs, L., Purser, S. J. D., et al. (2017). Gravitational instabilities in a protosolar-like disc - II. Continuum emission and mass estimates. *MNRAS* 470, 1828–1847. doi:10.1093/mnras/stx1365

Gammie, C. F. (2001). Nonlinear Outcome of Gravitational Instability in Cooling, Gaseous Disks. *ApJ* 553, 174–183. doi:10.1086/320631

Guillet, V., Girart, J. M., Maury, A. J., and Alves, F. O. (2020). Polarized emission by aligned grains in the Mie regime: Application to protoplanetary disks observed by ALMA. *A&A* 634, L15. doi:10.1051/0004-6361/201937314

Gundlach, B. and Blum, J. (2015). The Stickiness of Micrometer-sized Water-ice Particles. *ApJ* 798, 34. doi:10.1088/0004-637X/798/1/34

Hall, C., Dong, R., Rice, K., Harries, T. J., Najita, J., Alexander, R., et al. (2019). The Temporal Requirements of Directly Observing Self-gravitating Spiral Waves in Protoplanetary Disks with ALMA. *ApJ* 871, 228. doi:10.3847/1538-4357/aafac2

Harsono, D., van Dishoeck, E. F., Bruderer, S., Li, Z. Y., and Jørgensen, J. K. (2015). Testing protostellar disk formation models with ALMA observations. *A&A* 577, A22. doi:10.1051/0004-6361/201424550

Heywood, I., Avison, A., and Williams, C. J. (2011). The ALMA Observation Support Tool. In *Astronomy with Megastructures: Joint Science with the E-ELT and SKA*, Greece, 10-14 May 2010, eds. I. Hook, D. Rigopoulou, S. Rawlings, and A. Karastergiou. doi:10.48550/arXiv.1106.3516

Hsieh, C.-H., Arce, H. G., Maureira, M. J., Pineda, J. E., Segura-Cox, D., Mardones, D., et al. (2024). The ALMA Legacy Survey of Class 0/I Disks in Corona australis, Aquila, chaMaeleon, oPhiuchus north, Ophiuchus, Serpens (CAMPOS). I. Evolution of Protostellar Disk Radii. *ApJ* 973, 138. doi:10.3847/1538-4357/ad6152

Inutsuka, S.-i. (2012). Present-day star formation: From molecular cloud cores to protostars and protoplanetary disks. *Progress of Theoretical and Experimental Physics* 2012, 01A307. doi:10.1093/ptep/pts024

Jin, L. and Li, M. (2014). Diversity of Extrasolar Planets and Diversity of Molecular Cloud Cores. I. Semimajor Axes. *ApJ* 783, 37. doi:10.1088/0004-637X/783/1/37

Joos, M., Hennebelle, P., and Ciardi, A. (2012). Protostellar disk formation and transport of angular momentum during magnetized core collapse. *A&A* 543, A128. doi:10.1051/0004-6361/201118730

Jørgensen, J. K., van Dishoeck, E. F., Visser, R., Bourke, T. L., Wilner, D. J., Lommen, D., et al. (2009). PROSAC: a submillimeter array survey of low-mass protostars. II. The mass evolution of envelopes, disks, and stars from the Class 0 through I stages. *A&A* 507, 861–879. doi:10.1051/0004-6361/200912325

Kim, G., Lee, C. W., Maheswar, G., Kim, M.-R., Soam, A., Saito, M., et al. (2019). CO Outflow Survey of 68 Very Low Luminosity Objects: A Search for Proto-brown-dwarf Candidates. *ApJS* 240, 18. doi:10.3847/1538-4365/aaf889

Kóspál, Á., Cruz-Sáenz de Miera, F., White, J. A., Ábrahám, P., Chen, L., Csengeri, T., et al. (2021). Massive Compact Disks around FU Orionis-type Young Eruptive Stars Revealed by ALMA. *ApJS* 256, 30. doi:10.3847/1538-4365/ac0f09

Lam, K. H., Li, Z.-Y., Chen, C.-Y., Tomida, K., and Zhao, B. (2019). Disc formation in magnetized dense cores with turbulence and ambipolar diffusion. *MNRAS* 489, 5326–5347. doi:10.1093/mnras/stz2436

Lambrechts, M. and Johansen, A. (2012). Rapid growth of gas-giant cores by pebble accretion. *A&A* 544, A32. doi:10.1051/0004-6361/201219127

Lebreuilly, U., Commerçon, B., and Laibe, G. (2020). Protostellar collapse: the conditions to form dust-rich protoplanetary disks. *A&A* 641, A112. doi:10.1051/0004-6361/202038174

Liu, Y., Linz, H., Fang, M., Henning, T., Wolf, S., Flock, M., et al. (2022). Underestimation of the dust mass in protoplanetary disks: Effects of disk structure and dust properties. *A&A* 668, A175. doi:10.1051/0004-6361/202244505

Machida, M. N. and Basu, S. (2025). Complex Structure around a Circumstellar Disk Caused by Interchange Instability. *ApJL* 979, L49. doi:10.3847/2041-8213/adabc5

Manara, C. F., Ansdell, M., Rosotti, G. P., Hughes, A. M., Armitage, P. J., Lodato, G., et al. (2023). Demographics of Young Stars and their Protoplanetary Disks: Lessons Learned on Disk Evolution and its Connection to Planet Formation. In *Protostars and Planets VII*, eds. S. Inutsuka, Y. Aikawa, T. Muto, K. Tomida, and M. Tamura. vol. 534 of *Astronomical Society of the Pacific Conference Series*, 539. doi:10.48550/arXiv.2203.09930

Maury, A., Hennebelle, P., and Girart, J. M. (2022). Recent progress with observations and models to characterize the magnetic fields from star-forming cores to protostellar disks. *Frontiers in Astronomy and Space Sciences* 9, 949223. doi:10.3389/fspas.2022.949223

Mayer, L., Lufkin, G., Quinn, T., and Wadsley, J. (2007). Fragmentation of Gravitationally Unstable Gaseous Protoplanetary Disks with Radiative Transfer. *ApJL* 661, L77–L80. doi:10.1086/518433

McClure, M. K., Bergin, E. A., Cleeves, L. I., van Dishoeck, E. F., Blake, G. A., Evans, N. J., II, et al. (2016). Mass Measurements in Protoplanetary Disks from Hydrogen Deuteride. *ApJ* 831, 167. doi:10.3847/0004-637X/831/2/167

Mercer, A. and Stamatellos, D. (2020). Planet formation around M dwarfs via disc instability. Fragmentation conditions and protoplanet properties. *A&A* 633, A116. doi:10.1051/0004-6361/201936954

Meru, F. and Bate, M. R. (2012). On the convergence of the critical cooling time-scale for the fragmentation of self-gravitating discs. *MNRAS* 427, 2022–2046. doi:10.1111/j.1365-2966.2012.22035.x

Molyarova, T., Akimkin, V., Semenov, D., Henning, T., Vasyunin, A., and Wiebe, D. (2017). Gas Mass Tracers in Protoplanetary Disks: CO is Still the Best. *ApJ* 849, 130. doi:10.3847/1538-4357/aa9227

Nayakshin, S. (2017). Dawes Review 7: The Tidal Downsizing Hypothesis of Planet Formation. *PASA* 34, e002. doi:10.1017/pasa.2016.55

Ohashi, N., Tobin, J. J., Jørgensen, J. K., Takakuwa, S., Sheehan, P., Aikawa, Y., et al. (2023). Early Planet Formation in Embedded Disks (eDisk). I. Overview of the Program and First Results. *ApJ* 951, 8. doi:10.3847/1538-4357/acd384

Okuzumi, S. (2009). Electric Charging of Dust Aggregates and its Effect on Dust Coagulation in Protoplanetary Disks. *ApJ* 698, 1122–1135. doi:10.1088/0004-637X/698/2/1122

Ormel, C. W. and Cuzzi, J. N. (2007). Closed-form expressions for particle relative velocities induced by turbulence. *A&A* 466, 413–420. doi:10.1051/0004-6361:20066899

Ossenkopf, V. and Henning, T. (1994). Dust opacities for protostellar cores. *A&A* 291, 943–959

Pavlyuchenkov, Y., Akimkin, V., Wiebe, D., and Vorobyov, E. (2019). Revealing dust segregation in protoplanetary discs with the help of multifrequency spectral index maps. *MNRAS* 486, 3907–3914. doi:10.1093/mnras/stz1046

Pavlyuchenkov, Y. N., Zhilkin, A. G., Vorobyov, E. I., and Fateeva, A. M. (2015). The thermal structure of a protostellar envelope. *Astronomy Reports* 59, 133–144. doi:10.1134/S1063772915020067

Pezzuto, S., Elia, D., Schisano, E., Strafella, F., Di Francesco, J., Sadavoy, S., et al. (2012). Herschel observations of B1-bS and B1-bN: two first hydrostatic core candidates in the Perseus star-forming cloud. *A&A* 547, A54. doi:10.1051/0004-6361/201219501

Pollack, J. B., Hubickyj, O., Bodenheimer, P., Lissauer, J. J., Podolak, M., and Greenzweig, Y. (1996). Formation of the Giant Planets by Concurrent Accretion of Solids and Gas. *Icarus* 124, 62–85. doi:10.1006/icar.1996.0190

Rice, W. K. M., Armitage, P. J., Bonnell, I. A., Bate, M. R., Jeffers, S. V., and Vine, S. G. (2003). Substellar companions and isolated planetary-mass objects from protostellar disc fragmentation. *MNRAS* 346, L36–L40. doi:10.1111/j.1365-2966.2003.07317.x

Rosotti, G. P. (2023). Empirical constraints on turbulence in proto-planetary discs. *New Astron. Rev.* 96, 101674. doi:10.1016/j.newar.2023.101674

Santos-Lima, R., de Gouveia Dal Pino, E. M., and Lazarian, A. (2013). Disc formation in turbulent cloud cores: is magnetic flux loss necessary to stop the magnetic braking catastrophe or not? *MNRAS* 429, 3371–3378. doi:10.1093/mnras/sts597

Seifried, D., Banerjee, R., Pudritz, R. E., and Klessen, R. S. (2012). Disc formation in turbulent massive cores: circumventing the magnetic braking catastrophe. *MNRAS* 423, L40–L44. doi:10.1111/j.1745-3933.2012.01253.x

Shakura, N. I. and Sunyaev, R. A. (1973). Black holes in binary systems. Observational appearance. *A&A* 24, 337–355

Takahashi, S. Z., Tsukamoto, Y., and Inutsuka, S. (2016). A revised condition for self-gravitational fragmentation of protoplanetary discs. *MNRAS* 458, 3597–3612. doi:10.1093/mnras/stw557

Tobin, J. J., Sheehan, P. D., Megeath, S. T., Díaz-Rodríguez, A. K., Offner, S. S. R., Murillo, N. M., et al. (2020). The VLA/ALMA Nascent Disk and Multiplicity (VANDAM) Survey of Orion Protostars. II. A Statistical Characterization of Class 0 and Class I Protostellar Disks. *ApJ* 890, 130. doi:10.3847/1538-4357/ab6f64

Tomida, K., Okuzumi, S., and Machida, M. N. (2015). Radiation Magnetohydrodynamic Simulations of Protostellar Collapse: Nonideal Magnetohydrodynamic Effects and Early Formation of Circumstellar Disks. *ApJ* 801, 117. doi:10.1088/0004-637X/801/2/117

Toomre, A. (1964). On the gravitational stability of a disk of stars. *ApJ* 139, 1217–1238. doi:10.1086/147861

Trapman, L., Facchini, S., Hogerheijde, M. R., van Dishoeck, E. F., and Bruderer, S. (2019). Gas versus dust sizes of protoplanetary discs: effects of dust evolution. *A&A* 629, A79. doi:10.1051/0004-6361/201834723

Trapman, L., Longarini, C., Rosotti, G. P., Andrews, S. M., Bae, J., Barraza-Alfaro, M., et al. (2025). exoALMA. XIII. Gas Masses from N_2H^+ and C^{18}O : A Comparison of Measurement Techniques for Protoplanetary Gas Disk Masses. *ApJL* 984, L18. doi:10.3847/2041-8213/adc430

Tychoniec, Ł., Manara, C. F., Rosotti, G. P., van Dishoeck, E. F., Cridland, A. J., Hsieh, T.-H., et al. (2020). Dust masses of young disks: constraining the initial solid reservoir for planet formation. *A&A* 640, A19. doi:10.1051/0004-6361/202037851

Veronesi, B., Paneque-Carreño, T., Lodato, G., Testi, L., Pérez, L. M., Bertin, G., et al. (2021). A Dynamical Measurement of the Disk Mass in Elias 227. *ApJL* 914, L27. doi:10.3847/2041-8213/abfe6a

Viscardi, E. M., Macías, E., Zagaria, F., Sierra, A., Jiang, H., Yoshida, T. C., et al. (2025). Dust characterization of protoplanetary disks: A guide to multi-wavelength analyses and accurate dust mass measurements. *A&A* 695, A147. doi:10.1051/0004-6361/202452935

Vorobyov, E. I. (2013). Formation of giant planets and brown dwarfs on wide orbits. *A&A* 552, A129. doi:10.1051/0004-6361/201220601

Vorobyov, E. I., Elbakyan, V., Dunham, M. M., and Guedel, M. (2017a). The nature of very low luminosity objects (VeLLOs). *A&A* 600, A36. doi:10.1051/0004-6361/201628922

Vorobyov, E. I., Elbakyan, V., Hosokawa, T., Sakurai, Y., Guedel, M., and Yorke, H. (2017b). Effect of accretion on the pre-main-sequence evolution of low-mass stars and brown dwarfs. *A&A* 605, A77. doi:10.1051/0004-6361/201630356

Vorobyov, E. I., Elbakyan, V. G., Skliarevskii, A., Akimkin, V., and Kulikov, I. (2025). Dust enrichment and growth in the earliest stages of protoplanetary disk formation. *A&A* 699, A27. doi:10.1051/0004-6361/202553718

Vorobyov, E. I., Kulikov, I., Elbakyan, V. G., McKevitt, J., and Güdel, M. (2024). Dust growth and pebble formation in the initial stages of protoplanetary disk evolution. *A&A* 683, A202. doi:10.1051/0004-6361/202348023

Vorobyov, E. I., Matsukoba, R., Omukai, K., and Guedel, M. (2020). Thermal evolution of protoplanetary disks: from β -cooling to decoupled gas and dust temperatures. *A&A* 638, A102. doi:10.1051/0004-6361/202037841

Wada, K., Tanaka, H., Suyama, T., Kimura, H., and Yamamoto, T. (2011). The Rebound Condition of Dust Aggregates Revealed by Numerical Simulation of Their Collisions. *ApJ* 737, 36. doi:10.1088/0004-637X/737/1/36

Woitke, P., Min, M., Pinte, C., Thi, W. F., Kamp, I., Rab, C., et al. (2016). Consistent dust and gas models for protoplanetary disks. I. Disk shape, dust settling, opacities, and PAHs. *A&A* 586, A103. doi:10.1051/0004-6361/201526538

Wurster, J., Bate, M. R., and Bonnell, I. A. (2021). The impact of non-ideal magnetohydrodynamic processes on discs, outflows, counter-rotation, and magnetic walls during the early stages of star formation. *MNRAS* 507, 2354–2372. doi:10.1093/mnras/stab2296

Xu, W., Jiang, Y.-F., Kunz, M. W., and Stone, J. M. (2025). Global Simulations of Gravitational Instability in Protostellar Disks with Full Radiation Transport. I. Stochastic Fragmentation with Optical-depth-dependent Rate and Universal Fragment Mass. *ApJ* 986, 91. doi:10.3847/1538-4357/add14a

Zhu, Z., Zhang, S., Jiang, Y.-F., Kataoka, A., Birnstiel, T., Dullemond, C. P., et al. (2019). One Solution to the Mass Budget Problem for Planet Formation: Optically Thick Disks with Dust Scattering. *ApJL* 877, L18. doi:10.3847/2041-8213/ab1f8c

7 APPENDIX A. BASIC MODEL EQUATIONS

The dynamics of gas is followed by solving the equations of continuity and momentum

$$\frac{\partial \rho_g}{\partial t} + \nabla \cdot (\rho_g \mathbf{v}) = 0, \quad (4)$$

$$\frac{\partial}{\partial t} (\rho_g \mathbf{v}) + \nabla \cdot (\rho_g \mathbf{v} \otimes \mathbf{v} + \mathbb{I}P) = -\rho_g \nabla \Phi - \rho_{d,gr} \mathbf{f}, \quad (5)$$

where ρ_g is the volume density of gas, Φ is the gravitational potential, \mathbf{v} is the gas velocity, P is the gas pressure, \mathbb{I} is the unit tensor, and \mathbf{f} is the friction force per unit dust mass between gas and dust. We used a barotropic equation of state for the closure relation between the gas pressure and density, which smoothly links an isothermal envelope with the disk and accounts for rotational degrees of freedom of H₂ at temperatures exceeding ≈ 100 K (see Vorobyov et al., 2024, for details). The full energy balance equation is therefore not solved.

Dust is considered as a pressureless fluid having two populations: small dust that is dynamically linked to gas and grown dust that is dynamically decoupled from gas. The corresponding dust dynamics equations are

$$\frac{\partial \rho_{d,sm}}{\partial t} + \nabla \cdot (\rho_{d,sm} \mathbf{v}) = -S(a_{\max}), \quad (6)$$

$$\frac{\partial \rho_{d,gr}}{\partial t} + \nabla \cdot (\rho_{d,gr} \mathbf{u}) = S(a_{\max}), \quad (7)$$

$$\begin{aligned} \frac{\partial}{\partial t} (\rho_{d,gr} \mathbf{u}) + \nabla \cdot (\rho_{d,gr} \mathbf{u} \otimes \mathbf{u}) &= -\rho_{d,gr} \nabla \Phi + \rho_{d,gr} \mathbf{f} \\ &+ S(a_{\max}) \mathbf{v}, \end{aligned} \quad (8)$$

where $\rho_{d,sm}$ and $\rho_{d,gr}$ are the volume densities of small and grown dust, respectively, \mathbf{u} the velocity of grown dust, and $S(a_{\max})$ the conversion rate between small and grown dust populations as dust grows and transits from the small to grown population. We adopt a simple monodisperse model of dust growth according to Birnstiel et al. (2012) and the expression for $S(a_{\max})$ can be found in Vorobyov et al. (2024). The dust growth is halted at the fragmentation barrier $a_{\text{frag}} = \rho_g u_{\text{frag}}^2 / (3\alpha \rho_s v_{\text{th}} \Omega_K)$, where $u_{\text{frag}} = 5.0 \text{ m s}^{-1}$ is a threshold relative velocity of colliding dust grains, above which grain-to-grain collisions lead to destruction rather than to growth, Ω_K is the Keplerian angular velocity, $\alpha = 10^{-3}$ is the Shakura and Sunyaev (1973) turbulent parameter, v_{th} is the mean thermal velocity of gas, and $\rho_s = 3.0 \text{ g cm}^{-3}$ is the material density of dust grains. The drag force between dust and gas is calculated as

$$\mathbf{f} = \frac{\mathbf{v} - \mathbf{u}}{t_{\text{stop}}}, \quad (9)$$

where $t_{\text{stop}} = a_{\max} \rho_s / (\rho_g v_{\text{th}})$ is the stopping time.

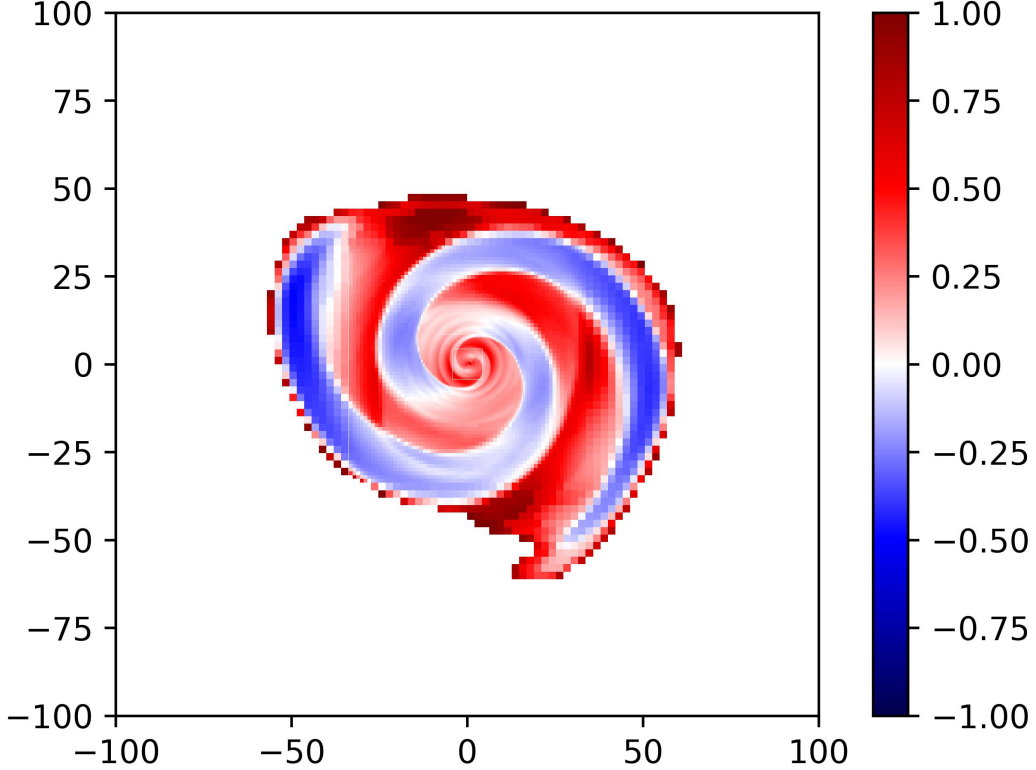


Figure 13. Two-dimensional map of the Q -parameter in the disk. The scale bar is in the log units.

8 APPENDIX B. TOOMRE Q -PARAMETER

To analyze the propensity of our model disk to gravitational instability, we calculate the Toomre Q -parameter (Toomre, 1964)

$$Q = \frac{c_s \Omega}{\pi G \Sigma_g}, \quad (10)$$

where c_s is the sound speed, Ω the angular velocity, G the gravitational constant, and Σ_g the surface density of gas. We neglect here a contribution of dust to the sound speed and local surface density, as the dust concentrations above the initial dust-to-gas ratio of 0.01 is small at these early stages of disk evolution. If $Q < 1$, the disk becomes unstable and develops a spiral pattern. If $Q < 0.6$ in the spiral arms, they can fragment to form compact gravitationally supported clumps (Takahashi et al., 2016).

As Figure 13 demonstrates, the Toomre-parameter in the spiral arms drops below unity, verifying the presence of gravitational instability. However, the Q -value also drops below the threshold for gravitational fragmentation in the outer parts of spiral arms ($Q \approx 0.5$), but fragments do not occur. This may be explained by the fact that the threshold criteria were derived for two-dimensional thin disks and require modifications to account for the three-dimensional disk structures. For instance, when deriving Σ_g we integrate over the entire disk extent rather than over one disk scale height. The use of angular velocity Ω in Eq. (10) is also valid only if it is well approximated by the Keplerian velocity, but this may not be so at this early stage of disk evolution in absence of a point-like gravity source.

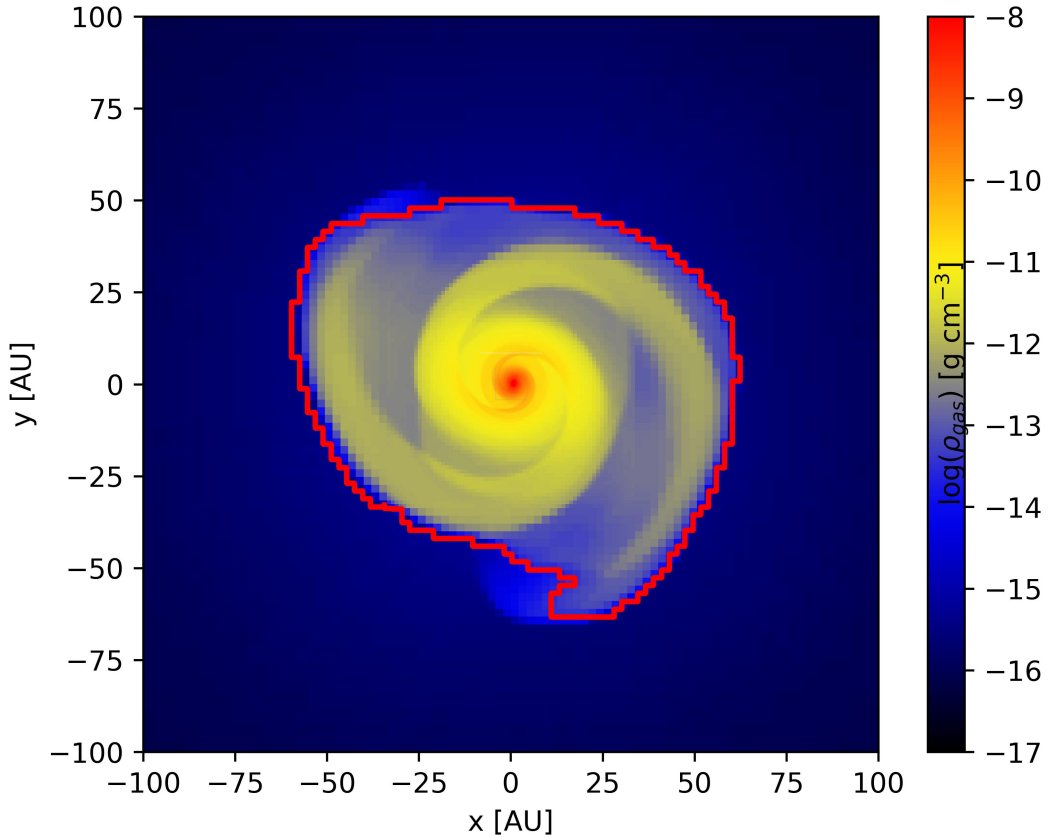


Figure 14. Distinguishing the disk from the infalling envelope. The red contour line indicates the disk outer boundary.

9 APPENDIX C. IDENTIFYING THE RADIUS OF THE MODEL DISK

Figure 14 presents the spatial map of the gas volume density in the disk midplane. The red contour line delineates the disk outer boundary according to the disk tracking mechanism of Sect. 3.1. As can be seen, the disk tracking mechanism distinguishes the disk from the infalling envelope (black low-density regions) fairly well. The azimuthally averaged disk radius is $R_{\text{mod}}^{\text{mod}} = 53$ au and the maximum extent of the disk at a specific azimuth is 66.5 au.

10 APPENDIX D. EFFECTS OF DUST SCATTERING

Figure 15 presents the azimuthally integrated radiation intensities in Band 6 obtained for the case of absorption opacity, neglecting the contribution from dust scattering. A comparison with Fig. 5 reveals that the radiation intensities of models with advanced dust growth ($a_{\text{max}} \geq 1.0$ mm) are characterized by shallower slopes, as in the case when scattering is also considered. However, I_{ν} in the inner 10–15 au is now of similar magnitude for all models regardless of a_{max} , whereas in Fig. 5 a significant drop in I_{ν} for models with $a_{\text{max}} \geq 1.0$ mm is evident. As was shown in Zhu et al. (2019), dust scattering modifies the radiation intensity in the optically thick limit as $I_{\nu} \sim \sqrt{1 - \omega_{\nu}} B_{\nu}(T)$, where $\omega_{\nu} = \kappa_{\nu, \text{sc}} / (\kappa_{\nu, \text{sc}} + \kappa_{\nu, \text{abs}})$ is the scattering albedo, and $\kappa_{\nu, \text{sc}}$ and $\kappa_{\nu, \text{abs}}$ are the scattering and absorption opacities. The former is much smaller than the latter for $a_{\text{max}} \leq 100$ μm , but becomes comparable to or greater than the absorption opacity as dust grows to $a_{\text{max}} = 1.0 - 10$ mm. This

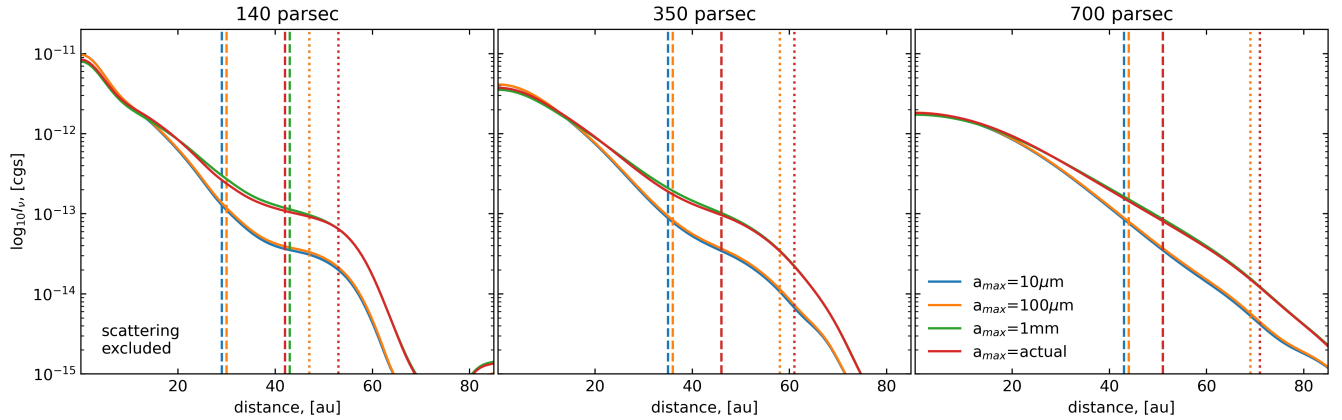


Figure 15. Similar to Fig. 5 but only for absorption dust opacity.

increases the scattering albedo and systematically lowers the radiation intensity and the integrated radiation flux in the advanced stages of dust growth, see Table 2.

11 APPENDIX E. DUST-SIZE-DEPENDENT OPACITIES

Figure 16 presents the dust absorption and scattering opacities at $\lambda = 1.3$ mm and 3.0 mm calculated with the opTool (Woitke et al., 2016). In particular, we fix the smallest size of dust grains at 5×10^{-3} μm , but vary the maximum dust size in the $10^{-3} - 10$ cm limits. The following dust composition is assumed: 40% – astrosilicates, 10% – foilite, and 50% – refractory organics. A sharp increase at the opacity cliff, $a_{\max} = \lambda/(2\pi)$, is evident.

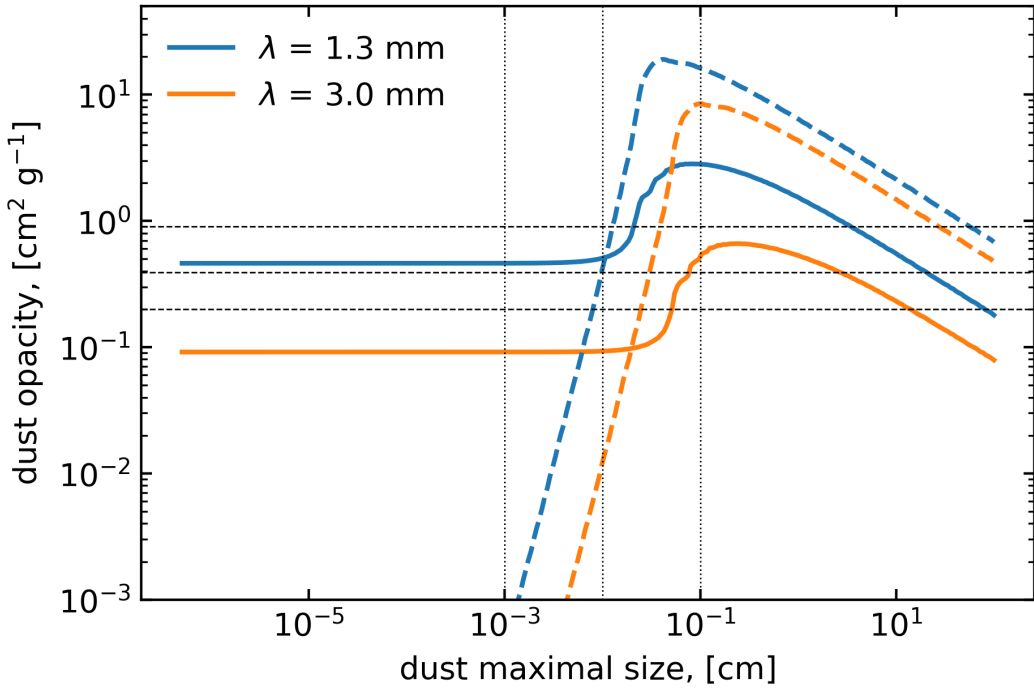


Figure 16. Dust absorption (solid lines) and scattering (dashed lines) opacity as a function of the maximum dust size a_{\max} . The vertical dotted lines identify the values of a_{\max} used in our work. The horizontal dashed lines are the Ossenkopf and Henning (1994) opacities considered in this work for Band 6 (top line) and Band 3 (middle and bottom lines).